IMPERIAL COLLEGE LONDON

Department of Earth Science and Engineering

Centre for Petroleum Studies

Quick Screening of Well Survivability in a Producing Reservoir

By

Justin Stephen Cassell

A report submitted in partial fulfillment of the requirements for the MSc and/or the DIC.

September 2014

DECLARATION OF OWN WORK

I declare that this thesis,

"Quick Screening of Well Survivability in a Producing Reservoir"

is entirely my own work and that where any material could be construed as the work of others, it is fully cited and referenced, and/or with appropriate acknowledgement given.

Signature: ……..……

Name of student: JUSTIN STEPHEN CASSELL

Name of academic supervisor: PROFESSOR MARTIN BLUNT

Name of industry supervisor: THOMAS BÉRARD

ACKNOWLEDGEMENTS

I wish to acknowledge and thank my Schlumberger supervisor, Thomas Bérard, for his guidance with this project. Despite his busy schedule he took the time to support the project for which I am grateful.

I would also like to thank Adrian Rodriguez Herrera for his help and continuous patience.

The Schlumberger Geomechanics Centre of Excellence provided me the means with which to complete this project for which I am thankful for. The guidance and discussions with the entire team has helped me to learn a great deal about geomechanics.

Lastly, I would like to thank Professor Martin Blunt for his advice and comments throughout the project.

Table of Contents

List of Figures and Tables

Imperial College
London

Quick Screening of Well Survivability in a Producing Reservoir

Justin Stephen Cassell

Professor Martin Blunt, Imperial College London

Thomas Bérard, Schlumberger

Abstract

Field-wide production-induced deformation over time, from a reservoir-geomechanical finite element model, is used as the input for geomechanical codes that calculate axial strain and shear strain along well trajectories. Threshold values for the onset of casing failure for both axial and shear strain are used to predict which wells and where are prone to casing collapse. These flags are compared against real field observations of casing deformations. The use of these geomechanical codes is to quickly scan projected wells in a field to flag which wells require intricate and time consuming wellbore scale finite element model analysis. This allows casings to be designed suitably. Casing and cement, and other completion details, are ignored in the geomechanical codes. Focusing on the deformations of large rock masses along a well's trajectory instead enables fast processing over numerous wells at many discrete time steps.

A field case containing 128 wells is used to test the application of the axial strain and shear strain geomechanical codes. In this field, 16 wells experienced casing deformation. Success of the implemented geomechanical codes depends on two conditions. Firstly, to match flagged well trajectories to deform with the observed casing deformations. Secondly, to flag the other 112 wells as experiencing no casing deformation. As casing deformation results from shearing, the focus was to analyze the shear strain results. In terms of the calculated shear strain, 92% of the deformed wells were correctly flagged to deform. Further analysis showed that 52% of the wells not experiencing deformation to be wrongly flagged to deform. In terms of axial strain, every well trajectory had a constricting and elongating strain less than the thresholds for material failure. It has been shown that wells can be scanned quickly on a field scale level based on the deformations of rock masses along trajectories but tend to over-estimate the risk of failure. Nonetheless, this method is able to identify which wells require countermeasures to ensure they do not experience casing deformation or failure.

Introduction

Fluid production and injection alters the pressure field in a reservoir. This affects the state of stress and leads to deformation in the reservoir as well as surrounding rock. These field wide changes can impact the integrity of wells and can ultimately result in their failure to provide access, isolation, and/or production means (Abou-Sayed et al, 2003).

A well-known example where casing failure became problematic was in the Ekofisk field. After 16 years of production, the sea floor subsided by 13 ft and caused two thirds of the wells to experience casing failure (Bruno, 1992). It was recorded that for every 33 ft of vertical movement there was a subsequent 3 ft of horizontal movement around the shoulders of the reservoir (Bickley et al, 1992).

The casing failures observed in the Ekofisk field were ultimately caused by the heavily compacting reservoir. As more fluids are produced, more of the overburden is supported by the rock matrix. This causes the rock to compact in the reservoir and to stretch in the overburden. This can cause the casing's material to fail through contraction in the producing interval or stretching in the overburden (Bruno, 1992). **Figure 1** shows that as a field compacts, the flexure of the compacting field can cause slippage along weak lithologies or discontinuities. This can cause structural failure through shearing of the casing. The shearing of a well's casing can also result from injection processes. Dusseault (1998) explained that high pressure injection can expand the reservoir. This can cause a reservoir to expand resulting in shearing along rock interfaces.

Currently, well survivability is analyzed on a field scale or on a wellbore scale. At the field scale, the total compaction and subsidence is calculated by analytical methods or through finite element models. This provides information whether well

trajectories are susceptible to high strains. Another method is analyzing the changing stresses and deformations on a wellbore scale to design a well's casing to ensure it can withstand local deformations.

Telles et al (2014) began identifying which wells on a field scale were prone to shearing based on knowledge of fault locations. This quick identification allows for appropriate casings to be implemented ensuring longevity. The proposed method of quick scanning for well survivability builds on this approach. The geomechanical codes developed incorporate simple wellbore scale detail of a well's azimuth and inclination along its entire trajectory. From the field scale model, the strain tensor from a reservoir-geomechanics simulation is used. This strain tensor is rotated by the azimuth and inclination to determine the axial strain and shear strain at intervals along each well trajectory in a field. Threshold values for the onset of deformation or failure are then combined to determine which wells and at what depth intervals may be susceptible to casing deformation or failure. The flagged wells are then compared to observed deformations in a field where 16 out of 128 wells were recorded to deform.

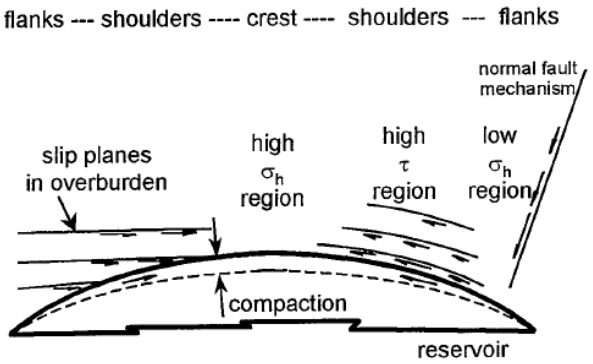

Figure 1: Flexure of a compacting field causes shearing along the shoulders of the reservoir (Dusseault, 1998).

Methodology

Current Methods in Determining Well Survivability

Field Scale

The simplest method in predicting well survivability in a field is with analytical methods. These are used as initial screening tools to assess broadly compaction related risks. An example is by incorporating the nucleus of strain equations developed by Geertsma. This method calculates the total subsidence at the surface from a compacting reservoir. This technique, however, considers the field to be homogeneous with a simple geometrical representation of a reservoir (Geertsma, 1973). Nonetheless, this technique can assess whether wells are at risk to casing failure with a linearly elastic behaviour of the overburden (Bruno, 2001).

A more detailed approach to identify casing failure risk on a field scale is by using finite element models (FEM). For a FEM, a 3D Mechanical Earth Model (MEM) is first constructed from data stemming from logs, seismic, core samples and drilling data. This information provides pore pressure, stresses and deformation of the formation at initial conditions. This geomechanical model is then coupled to a reservoir simulator. The reservoir simulator calculates the changes in fluid pressure, temperature and saturation. At defined time steps, this information is passed to the geomechanical model to update the in-situ stresses and rock deformations. In turn, this information is relayed back to the reservoir model to update permeability. The steps of this loosely coupled simulation are further outlined in Appendix C. This coupled simulation is repeated for prescribed number of time steps. The geomechanical simulator, VISAGE, uses a finite element model in conjunction with the elasto-plastic method to describe rock behavior and to update the stresses and deformations in the geomechanical model (Petrel Reservoir Geomechanics Software).

Appendix D outlines the fundamentals of the geomechanical model with description of a linear elastic model. The outputs of the strain tensor of this process are used as the inputs for the implemented geomechanical codes.

Wellbore Scale

To assess the survivability of a well's casing and completion design, a refined segment model is extracted from the field model. This is required as incorporating casing detail on a large scale in the field scale model is not an accurate means to

assess whether the well is prone to casing failure. The scale of a field model grid cells are on the order of 10's of feet whilst the scale of casing design is on the order of 10's of inches (Bruno, 2001).

After a well sector model is extracted and locally refined, the field scale results are used as boundary conditions. Subsequently, the well path is excavated with the details of the well's architecture and completion included. The integrity of the well is then assessed by simulation over defined time steps with the elastic and plastic strains of the casing and cement analysed (Geomechanics CoE, Schlumberger). However, this method is computationally demanding, data intensive and requires significant amounts of time, data and expertise. A detailed diagrammatic example of this process can be found in Appendix E.

Axial Strain and Shear Strain Geomechanical Codes

The proposed method for quick screening of well survivability incorporates the complexity of a field scale model with simple well sector detail. The well sector detail includes the inclination and azimuth of the trajectories of all wells in a field. The axial strain and shear strain along each trajectory will be produced. The measured strains are based on deformations of large rock masses. As a result, the strain tensor from the reservoir-geomechanical model, which was produced in previous work, along with the inclination and azimuth of each well are used for the implemented geomechanical codes. By not including complex well sector detail, it is possible to quickly scan many wells in a field. The objective is to use the shear strain and axial strain geomechanical codes at the first stage of well planning and flag wells and their intervals prone to casing collapse.

$$\tilde{\varepsilon} = \begin{pmatrix} \varepsilon_{xx} & \gamma_{xy} & \gamma_{xz} \\ \gamma_{yx} & \varepsilon_{yy} & \gamma_{yz} \\ \gamma_{zx} & \gamma_{zy} & \varepsilon_{zz} \end{pmatrix}$$

Eq. 1

$$\varepsilon' = \left[R_y(incl) \times R_z(azi)\right]^T \times \tilde{\varepsilon} = \begin{pmatrix} \varepsilon'_{xx} & \gamma'_{xy} & \gamma'_{xz} \\ \gamma'_{yx} & \varepsilon'_{yy} & \gamma'_{yz} \\ \gamma'_{zx} & \gamma'_{zy} & \varepsilon'_{zz} \end{pmatrix}$$

Eq. 2

Axial and shear strain are calculated at a defined sampling rate along a well's trajectory. The strain tensor, given in geographical coordinates, is rotated onto the well's local coordinate system at every measured point. **Figure 2** shows the field's coordinate system rotated onto a local point on a well's trajectory where it remains in relation to its top of hole (TOH). Eq. 1 is the strain tensor in the model's geographical coordinate system. It is rotated by the well's inclination and azimuth angles (Harrison et al, 1997). Eq. 2 shows this step where ε' is the rotated strain tensor on a point along a well's trajectory.

As the strain tensor is rotated based on its TOH, the zz component of the strain tensor is aligned with the well's trajectory. As a result, the ε'_{zz} in Eq. 2 is the axial strain at a given point along the well's trajectory. A positive value indicates an elongating strain with a negative value representing a contracting strain.

The measured shear strain at points along a well's trajectory is perpendicular to its axial strain. The shear components of γ_{xz} and γ_{yz} in Eq. 2 are used to find the resultant shear strain. Only the shear strains in relation to the well's axis (z-axis) are used to determine the resulting shear strain of a point along the well.

See Appendix F for details of how both strains are determined. The implemented code automatically calculates the axial and shear strain along each well in a field, provided a list of well names is inputted into the geomechanical code. The inclination, azimuth and strain tensor at every 5 ft MD, for each well, are used as inputs into the code. As a result, the axial and shear strain are calculated at increments of 5 ft MD along each well. Smaller sampling rates for calculation were found to substantially increase the time to produce the axial and shear strain results along each well. The sampling rate used was a balance between speed of processing whilst still capturing enough detail of the deforming rock masses. Appendix G shows the detail behind the implemented program with its code of how to calculate axial and shear strain.

Analyzing survivability along a line trajectory has its limitations. During a wellbore scale analysis, the well trajectory is excavated with casing and completion detail incorporated. Different types of casing and cement in addition to an applied mud will behave differently when affected by changing stresses. The type of casing joints will also have an effect when a well may experience casing collapse. As a result, the near wellbore stresses acting on the casing and excavated well is different than the stresses acting on a line source trajectory. In order to analyze which wells are susceptible to failure quickly, this level of detail

is excluded. This means a truer representation of the stresses and deformations acting on a well, with a certain diameter and casing strength, are not developed.

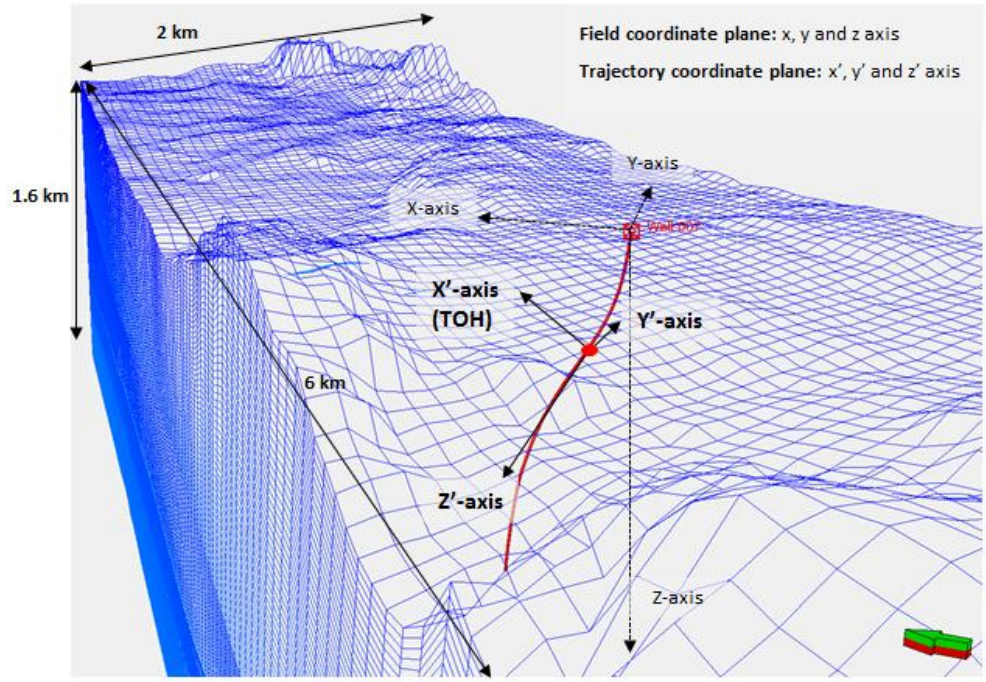

Figure 2: Comparison between geographical coordinate system and local coordinate system at one point on a well's trajectory.

Threshold Values for Onset of Failure

To process the results produced from the geomechanical codes, threshold values are needed for axial strain and shear strain for when failure occurs. Predicted failures are then compared to wells with observed casing deformations. This will provide success rates for the geomechanical codes in picking up failures and ultimately their usefulness in quickly analyzing well survivability. Appendix H shows tables reviewing threshold values found in literature.

Threshold values from observations of casing failure in the Magnolia field will be used for contraction and tension as demonstrated by Ibekwe et al. A range of 1% to 2.5% axial contraction saw increasing likelihood of failure. In terms of the stretching threshold, the same range was observed but for elongation of the well (Ibekwe et al, 2003). This range of 1% to 2.5% for both axial contraction and elongation will be used for analysis. The casing of a well is able to withstand a higher degree of compression than tension. However, literature is limited in the way of obtaining a more characteristic threshold value for the onset of tensile failure through stretching of the casing. The casing grade will have an effect when material failure occurs. This is why other researchers such as Bruno (1992) uses a more conservative threshold for the onset of failure through contraction with a range of 0.3% to 0.7%.

The maximum axial strain before failure is common in the literature unlike the threshold value for shear strain. The reason being is that the relationship that links the Young's Modulus of the casing and the stress and strain experienced by the casing involves the longitudinal (or axial) strain as it focuses on axial deformation (Rahman et al, 1995).

The proposed threshold value for onset of shear failure is based on history matching with the data as there is no value found in literature. However, the well casings in this field were only seen to deform. The minimum shear strain that was observed to cause casing deformation is used as the threshold value. This minimum value observed is 0.022% shear strain. This was recorded in Well-059 in which it deformed in 2009. As the analysis is focusing on wells deforming by 2009, this threshold provides an accurate means to analyze the results. This value is based on wells where a deformation interval coincided with a local sharp increase in shear strain. This means wells with depth mismatches and others with no apparent increase in shear strain were not included. The reason why this threshold is two magnitudes lower than the axial strain threshold will be reviewed in the discussion. It is plausible that some of the wells may have deformed by other mechanisms. This can affect the threshold used and ultimately the success of correctly flagging the wells known to deform.

Field Test Case

Geology

The field used to test the proxies is an onshore field that has surface dimensions of 6 km by 2 km. The reservoir consists of two sandstone intervals separated by a chert and shale layer. The upper and lower sandstone sections have a thickness of 113 m and 122 m respectively with the chert/shale interval being 45 m thick. The top of the reservoir is between 550 m deep to 1000 m deep in places. Before production took place, both the upper and lower sections of the reservoir were under pressured.

Coupled Reservoir-Geomechanics Model

The strain tensor from a pre-constructed reservoir-geomechanics model is used. The 3D MEM was initialized to the year 2000. Production began in 2003 with subsequent injection following in 2006. Field wide stresses and strains were calculated at two coupled time steps of 2006 and 2009 in a previous project (Geomechanics CoE, Schlumberger). The field being used has 102 producing wells and 26 water injection wells. **Figure 3** shows the pore pressure and vertical strain at both coupled time steps. By comparing the pressure field and vertical strain field it can be seen that the reservoir expands caused by injection with producing areas experiencing compaction.

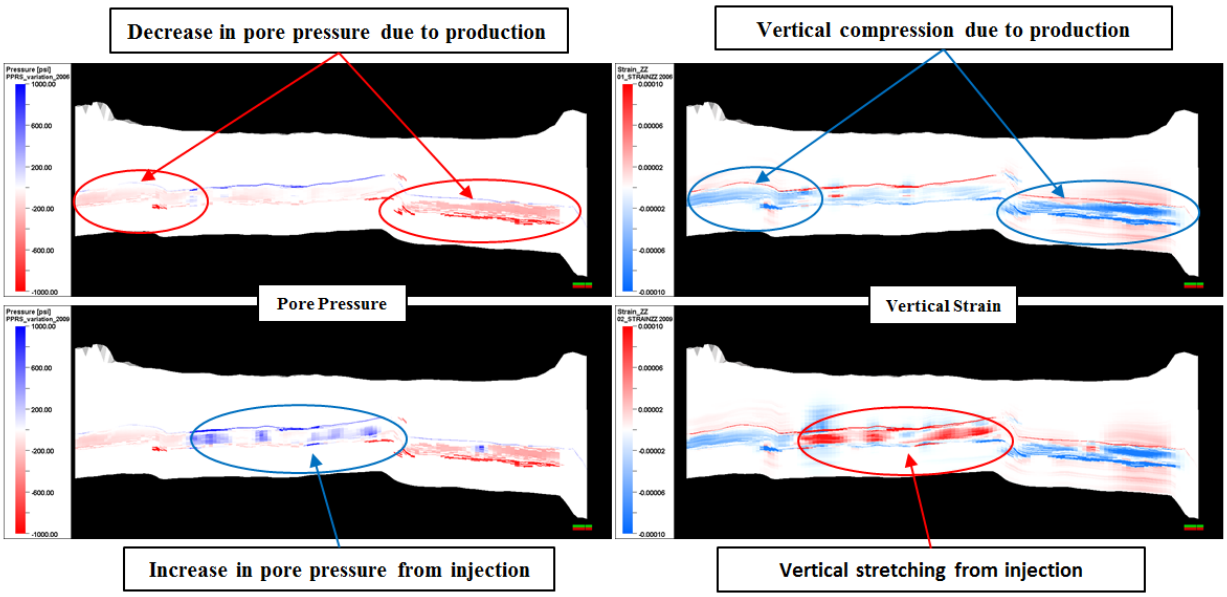

Figure 3: Comparison between the changes in pore pressure and vertical strain in the two coupled time steps of 2006 (top) and 2009 (bottom).

Observed Casing Deformations

In total, 16 wells experienced deformation. Each deformation was located with a multi-caliper tool along the chert and lower sandstone interface or in the close vicinity of this interface. From the detailed analysis report (Geomechanics CoE, Schlumberger), it is suggested that the probable cause of casing collapse was the water injected into the reservoir but going into the chert interval. The water injection reduced the chert's Young's Modulus by 45% and reduced its cohesion by 40%. The varied Young's Modulus and cohesion were incorporated into the geomechanical model that was used. However, their values are not considered to vary over time in the model. Usually, varying mechanical properties over time are included. In this case, the final reduction is used as the initial values in the model. **Figure 4** shows the casings for three of the deformed wells where they deformed by up to 3 inches. The length of the deformation intervals were seen to range from 1 to 23 ft long.

Since the injection program began in 2006, there has been a recorded casing deformation in every year up to 2010. Nine of the recorded deformations occurred in 2009. Only three wells were observed to deform beyond 2009, in 2010. No information is available for wells that deformed post 2010 resulting from the casing collapse project ending in 2011. It should be noted that there is also no information based on the frequency or extent of using multi caliper tools to identify deformed wells across the entire field.

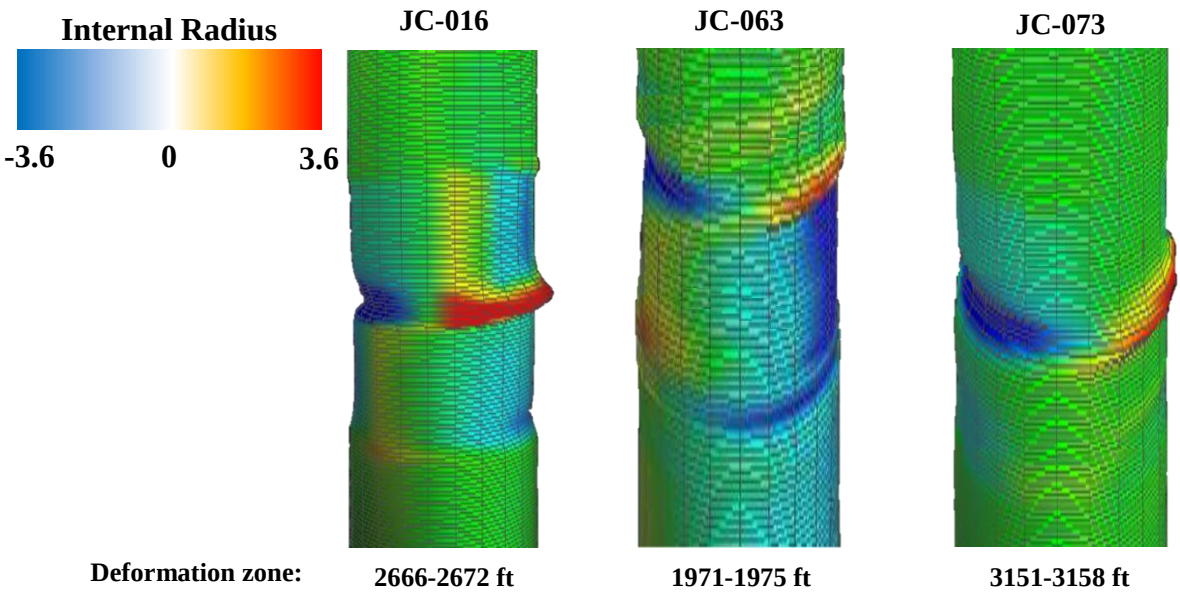

Figure 4: Shearing deformations along three wells (Geomechanics CoE, Schlumberger).

Results

The axial strain and shear strain along the trajectories for all 128 wells were calculated in 12 minutes. A well log containing the calculated axial and shear strain was produced for each well in the field.

Figure 5 shows the results of the axial and shear strain from the 2009 time step along the well trajectories of both deformed wells and non-deformed wells. The 'red' log along this trajectory is the shear strain with the 'blue' log representing axial strain. It shows that there is axial stretching within the injected interval. Intervals of high shear strain coincide with observed casing deformation with some non-deformed wells also experiencing intervals of high shear strain.

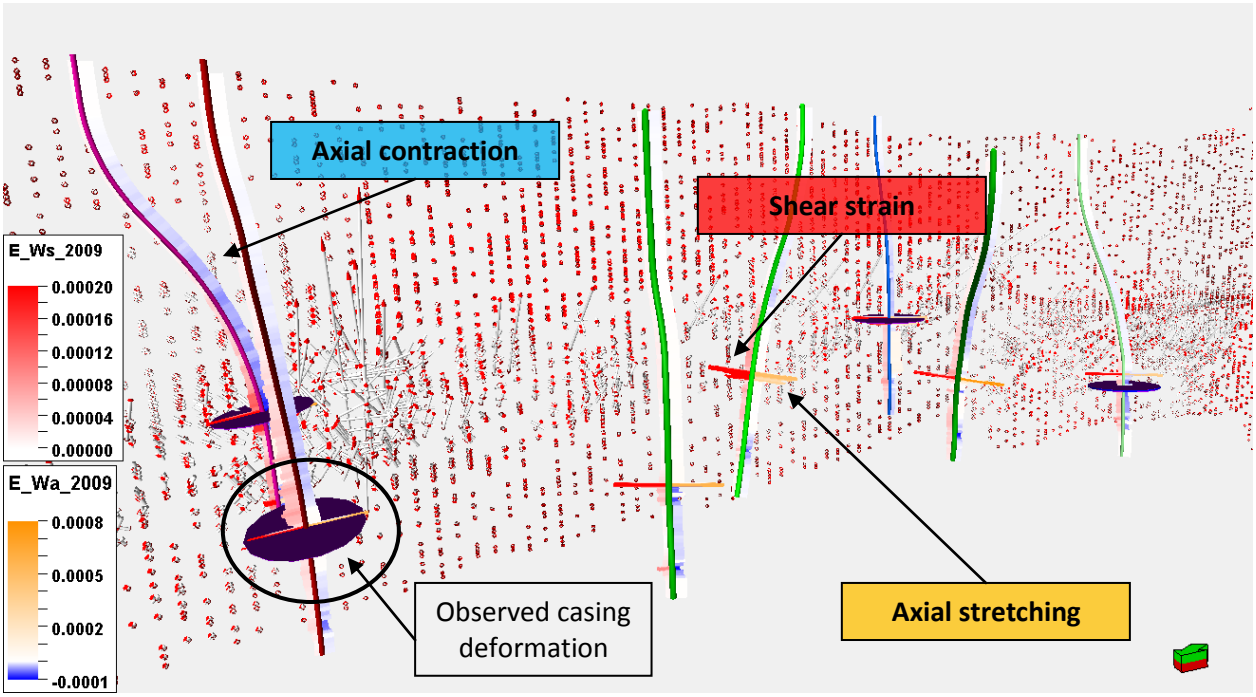

Figure 5: Axial and shear strain along a well's trajectory in an ambient strain field with the deformation interval highlighted.

Well Log Results

Figure 6 shows the axial and shear strain results for 2006 (dashed lines) and 2009 (solid lines) in a well log format. These results are shown across both producing sandstone intervals with the chert/shale interval marked by the red zone in the lithology band. The purple intervals in the left track of each log represent the observed deformation and its depth is based on information from the multi-caliper readings. Appendix I shows the results of the other 10 deformed wells that were observed to deform before 2009.

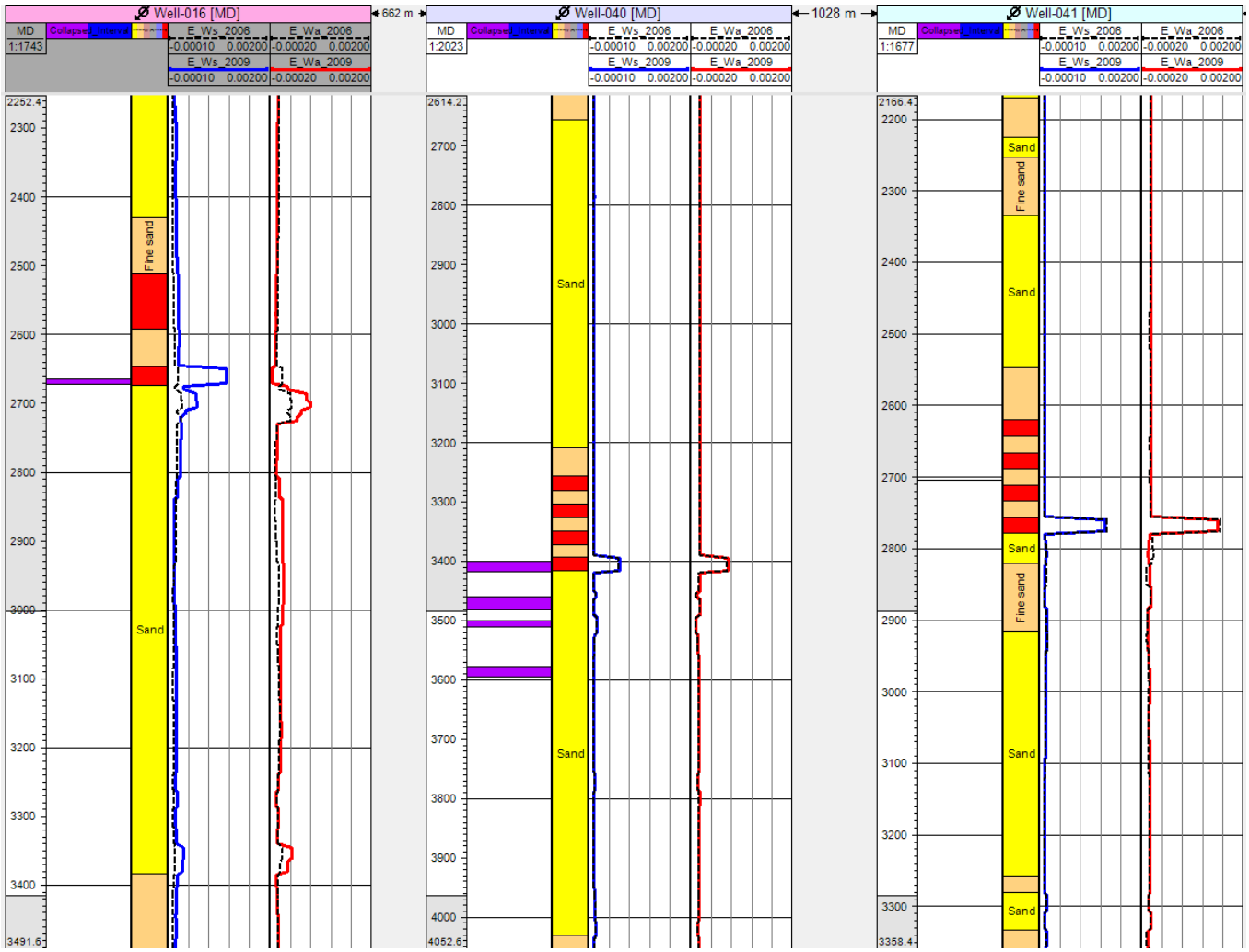

Figure 6: Well log results for three wells showing the shear strain and axial strain from two coupled time steps of 2006 and 2009.

Orientation and Time Effects

Figure 7 shows shear strain along the trajectories of three wells in an isotropic strain field. It shows that shear strain increases when the well becomes inclined. A vertical well only experiences the principal strains in each grid cell. When this well intersects a grid cell at an angle, the shear components of the strain tensor are induced. The relation between normal strains and shear strains is explained by Mohr's circle in Appendix J.

Figure 8 shows that large shear strains are not induced where inclination angle is at its highest in an anisotropic strain field. They are experienced near the bottom of the well where inclination is less than 6˚. This is caused by the strain tensor being much larger in the producing interval, particularly near the chert interval, than in the overburden. In an anisotropic strain field, the shear strain along a well's trajectory will be affected by its azimuth.

Figure 9 shows the time effects on the calculated shear strain and axial strain in 2006 and 2009. Well-136 in Figure 9 was observed to deform in 2009. Based on this figure, it shows that this well would not experience deformation in 2006. This is in

agreement to observations from the field. However, for a number of wells, deformations recorded in 2009 would be flagged based on the strain results in 2006.

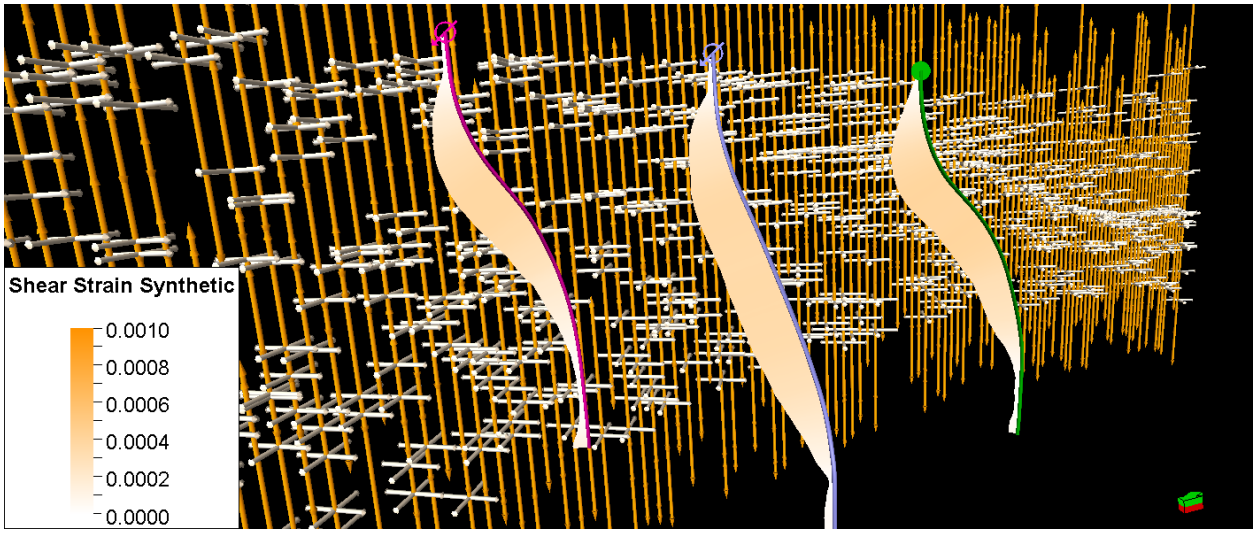

Figure 7: The effect of inclination angle on shear strain in an isotropic strain field.

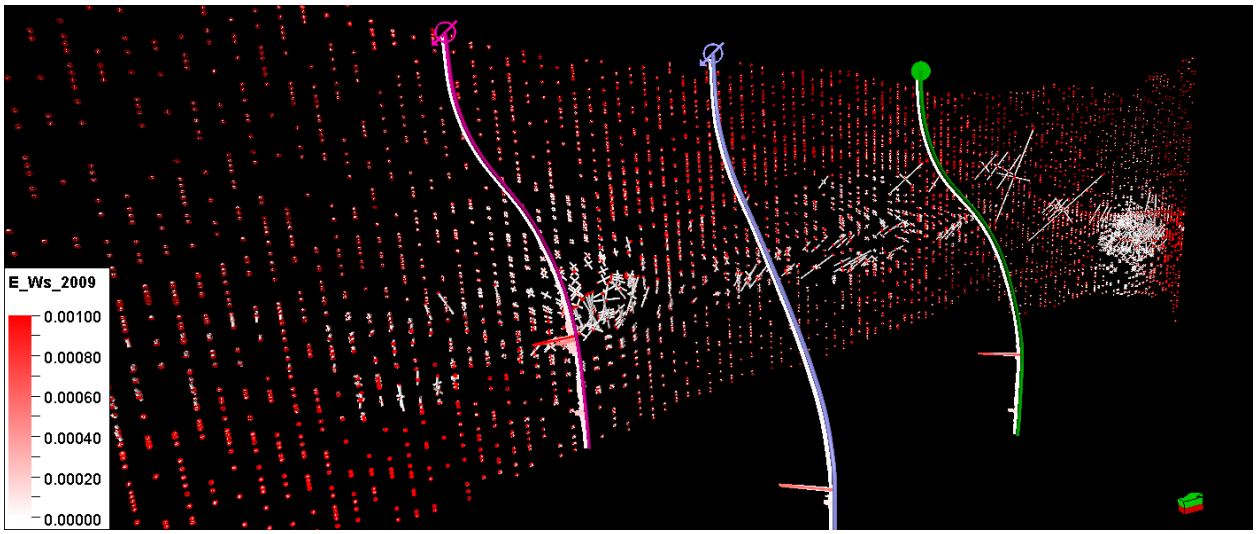

Figure 8: Shear strain along the well trajectories in an anisotropic strain field.

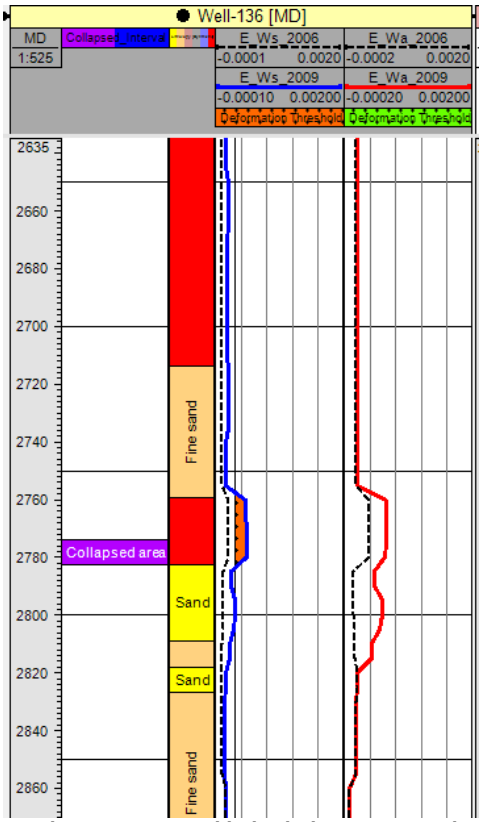

Figure 9: The shear strain and axial strain results are compared in both time steps. It shows that in 2006 this well would not deform based on the threshold (*Well-136 deformed in 2009*).

Analysis

Success of Axial and Shear Strain Geomechanical Codes

Upscaling

To determine the success of using the axial strain and the shear strain geomechanical codes to predict casing deformation, the well log results were upscaled. This provides one value of axial strain and one value of shear strain per grid cell. The average size of a grid cell in the producing interval has a height of 11 m with a width and depth of 50 m. Grid cells near the chert interval, where deformations occur, have dimensions 0.50 m for height with a width and depth of 50 m. The deformation intervals were also upscaled. This means analysis could be performed to calculate the percentage of grid cells that would deform based on the thresholds provided.

The reason why upscaling was required was down to the sampling rate in which the axial strain and shear strain were calculated at. The sampling rate was at every 5 ft MD. This means that within one grid cell there would be a number of calculated points of axial and shear strain. Furthermore, multiple data points lay within a deformation interval. So, a deformed interval could not be related to one consistent value of shear strain along its depth.

Figure 10 shows the result of this upscaling where only the cell blocks intersected by the trajectory of a well is displayed. Each one of these grid cells contains one averaged axial strain and shear strain. The upscaling technique used was arithmetic averaging. It was checked that the upscaled results did not differ to a large extent from the actual well log results.

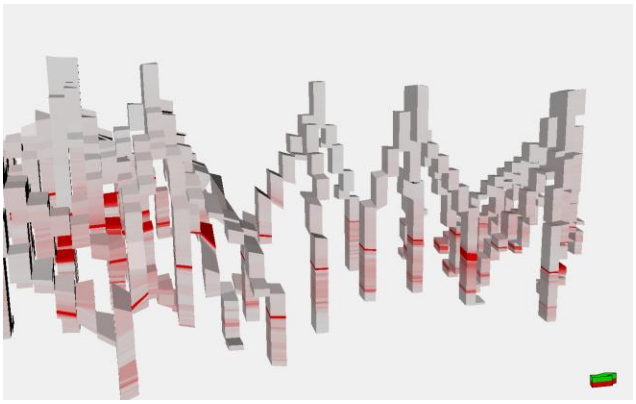

Figure 10: Upscaling of the shear strain well logs into the model provides one shear strain per cell.

Axial Strain

Figure 11 is a histogram showing the frequency of axial strain along all deformed grid cells intersected by well trajectories. The results are displayed in fractions, so the point at which casing failure occurs is at 0.01 axial strain. With the incorporation of the threshold values for the onset of casing failure it is seen that the calculated axial strain is within the indicated shaded failure zones in Figure 11. The axial strain results were also analyzed based on grid cells not seen to deform. **Figure 12** shows that all of the non-deformed grid cells do not go beyond the point of failure. This means no well is predicted to experience casing failure.

If the axial strain along a well's trajectory is a contributing factor to casing deformation, or if it is the main cause, then this method fails as it identifies no grid cell to deform based on its axial strain. However, from previous work done on this field, it was concluded that the casings of the wells deformed through shearing (Geomechanics CoE, Schlumberger). As a result, with no grid cells flagged, the application of the axial strain geomechanical code with threshold values can be regarded as a success.

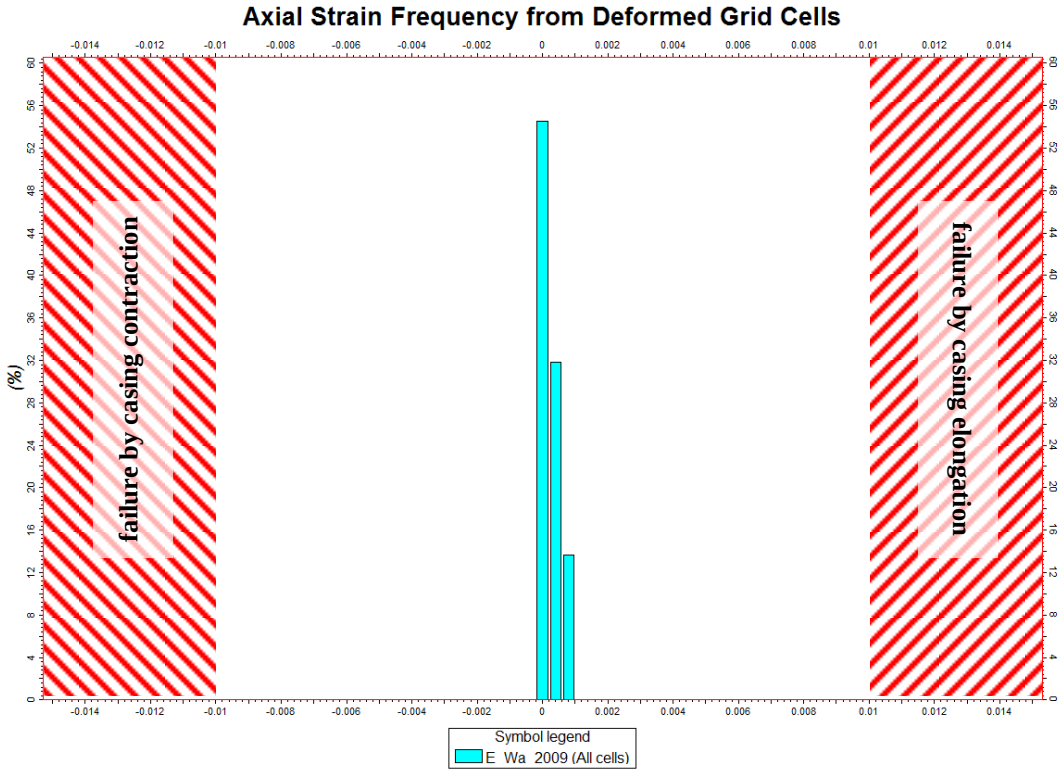

Figure 11: Histogram showing the frequency of axial strain (as a fraction) along all deformed grid cells. The shaded areas indicate where failure through contraction or stretching occurs.

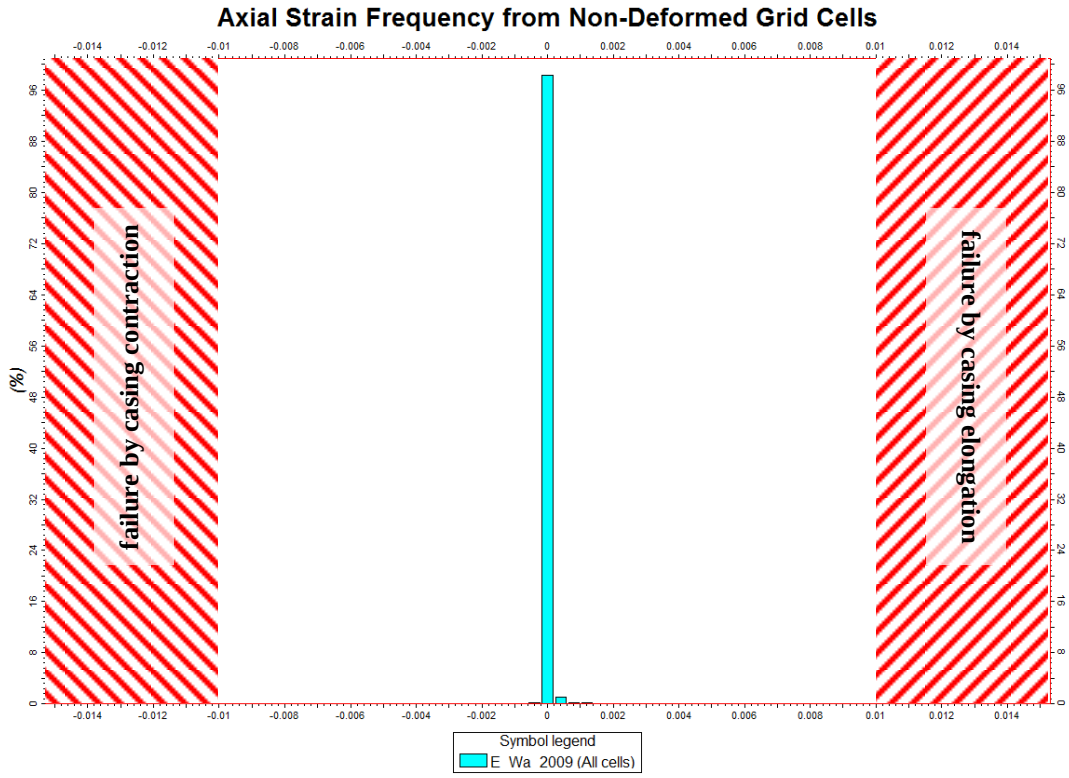

Figure 12: Histogram showing the frequency of axial strain (as a fraction) along all non-deformed grid cells. The shaded areas indicate where failure through contraction or stretching occurs.

Shear Strain

Figure 13 is a histogram showing the frequency of shear strain along non-deformed grid cells. Again, the strain fractions are used in the subsequent histograms. The red zone indicates where deformation would occur. This means 1.4% of the total number of grid cells would be wrongly identified to deform based on the deformation threshold. From well log analysis, this translates to 59 out of the 112 wells by 2009 to be wrongly flagged to deform. This means 52% of the wells not to have been observed to deform are wrongly flagged.

Figure 14 is another histogram that only shows the frequency of shear strains along deformed grid cells. The main hypothesis would be that wells observed to deform would be flagged to deform based on the shear strain results along every well. However, this figure shows that only 45% of grid cells are flagged correctly for deformation. This means that 55% of the deformed grid cells would not be flagged. Furthermore, large frequencies of overlooked grid cells occur between 0 and 0.01% shear strain. So even if the threshold decreased, a large number of grid cells not flagged will still exist. However, if the results from the well logs are analyzed then 12 out of 13 wells known to deform were correctly flagged to deform.

From analyzing well logs, it is clear that the low success of flagging grid cells to shear is resulting from three causes. Firstly, for two wells, there is a depth mismatch between recorded deformation and area of shear strain flagged to deform. An example of this is shown in **Figure 15**. Secondly, **Figure 16** shows an example where shear strain at a point of deformation is not flagged to deform based on its low shear strain and threshold value used. This occurs once with the upscaled results. Lastly, **Figure 17** shows that for a well with multiple deformation intervals, only one deformation may have an associated shear strain high enough to cause deformation. This observation occurs in two wells. For all of these examples the upscaled results were used to be consistent with the statistical analysis.

Figure 18 shows the success results if different values for the threshold for deformation are used. The percentages are based on the threshold values used in **Table 1**. The results in Table 1 show that if 100% of the deformed grid cells were to be correctly flagged to shear, then 100% non-deformed grid cells would be wrongly flagged to deform. Figure 18 shows that if the threshold is decreased, then the percentage of wrongly flagging wells increases substantially with more intervals per well in the overburden and underburden also flagged for deformation. If the threshold for deformation is increased, there is still a significant portion of the non-deformed wells to be falsely flagged. Furthermore, the percentage of flagging wells known to deform decreases. The threshold chosen is a balance between correctly flagged wells and wrongly flagged wells.

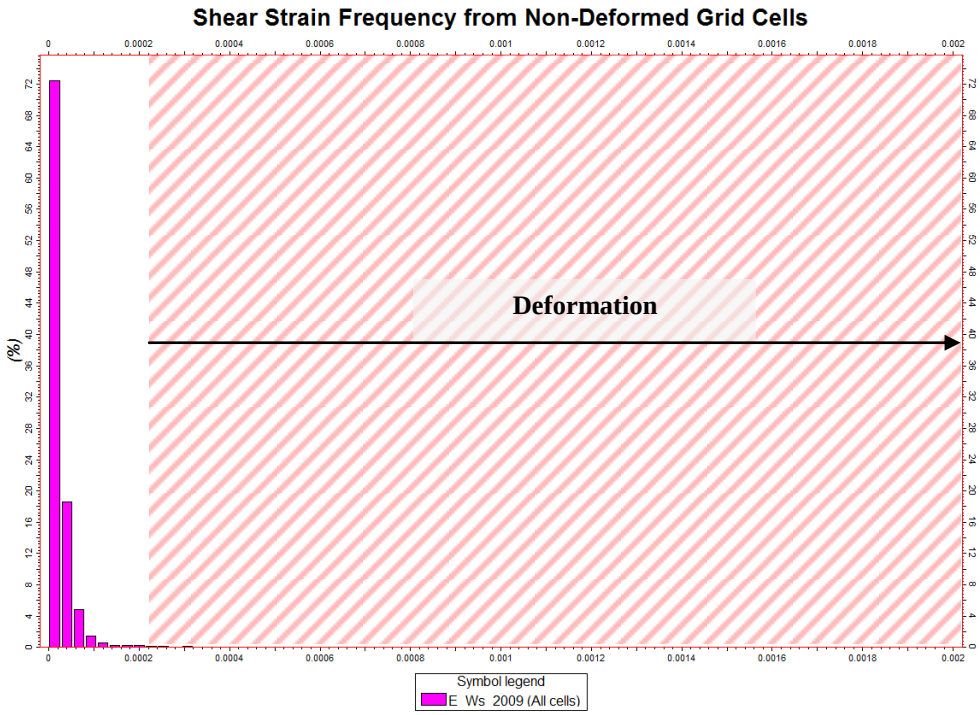

Figure 13: Histogram showing the frequency of different shear strains (as fractions) along all non-collapsed grid cells. 1.4% of strains exceed the threshold for deformation.

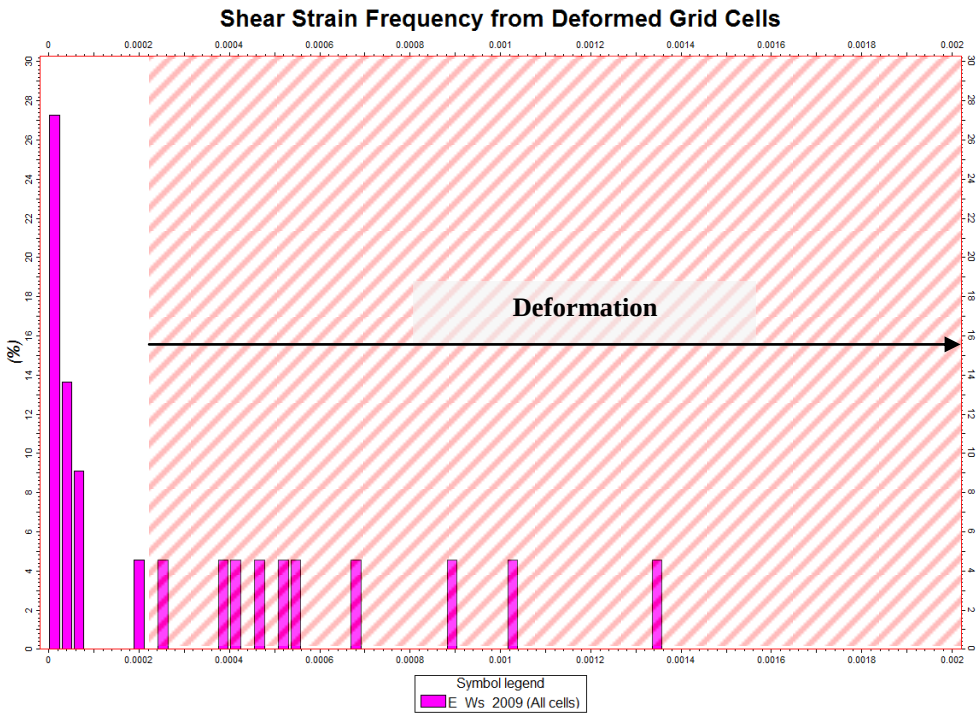

Figure 14: Histogram showing the frequency of shear strain (as fractions) along deformed grid cells. 45% of shear strains would be flagged based on the deformation threshold.

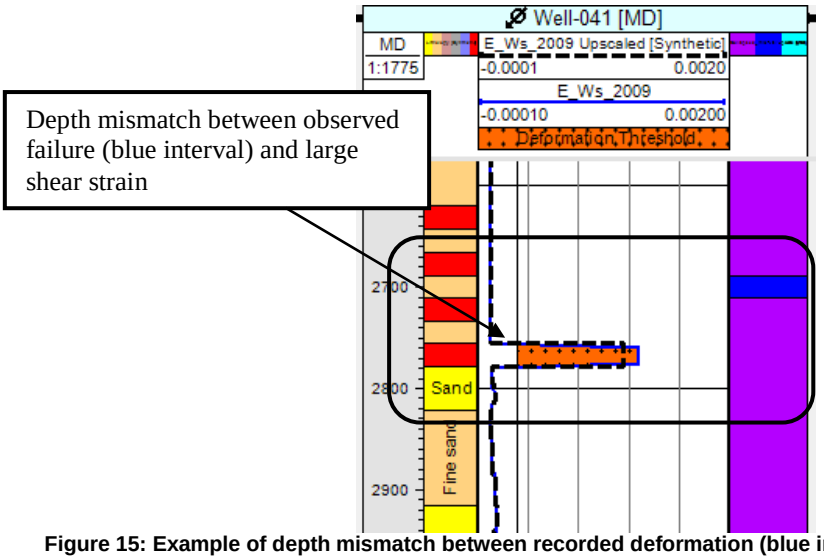

Figure 15: Example of depth mismatch between recorded deformation (blue interval) and high shear strain.

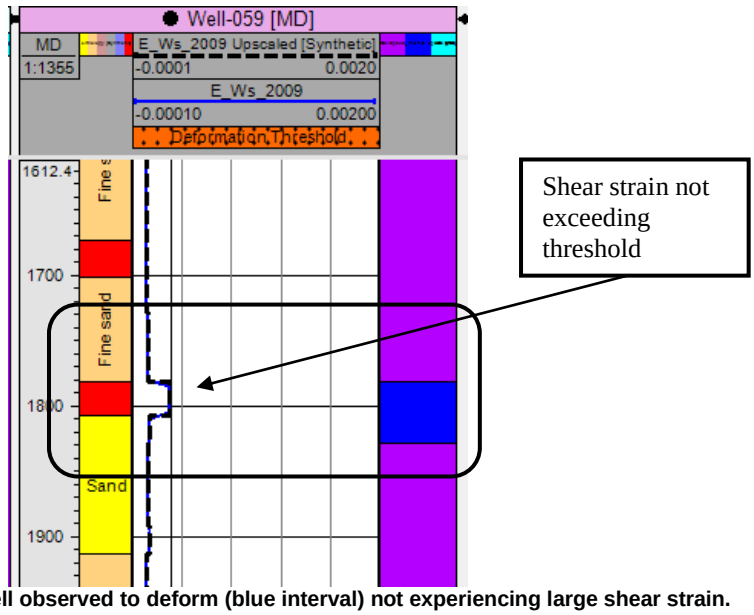

Figure 16: Example of well observed to deform (blue interval) not experiencing large shear strain.

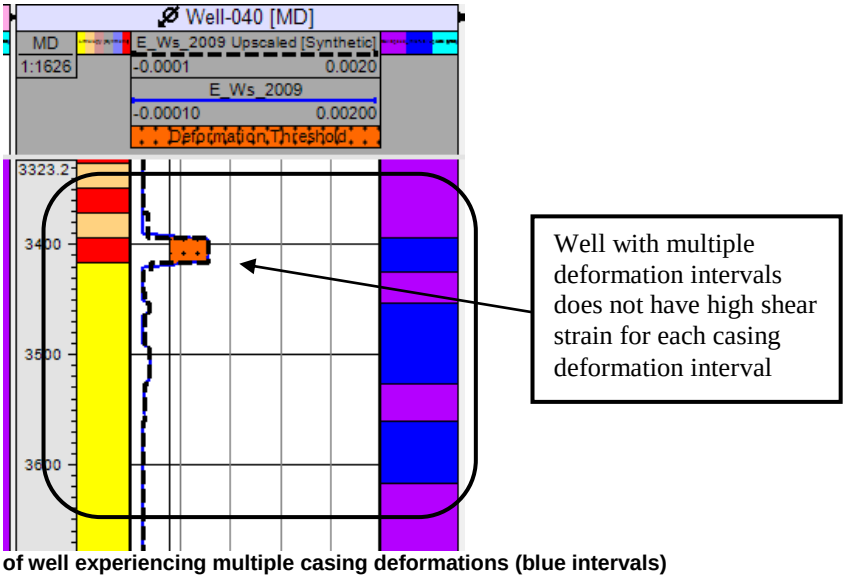

Figure 17: Example of well experiencing multiple casing deformations (blue intervals)

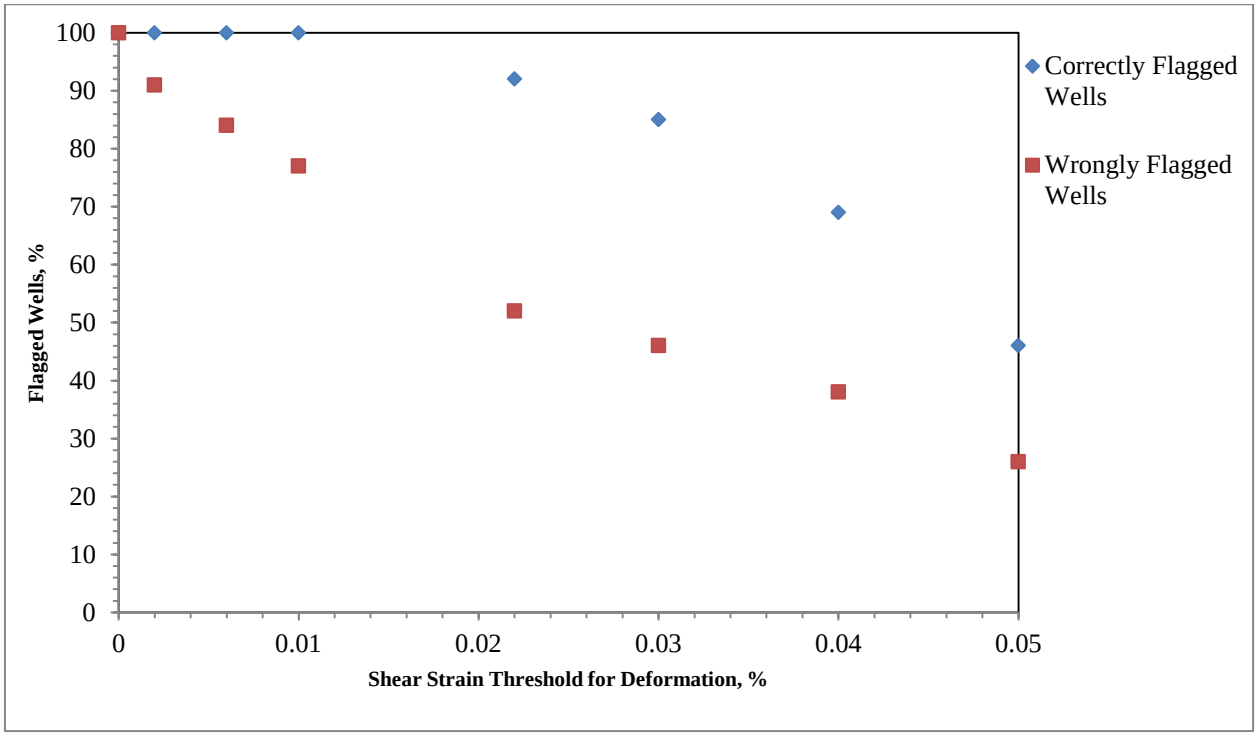

Figure 18: Comparison between correctly flagged wells to deform and wrongly flagged wells to deform with different thresholds.

Table 1: Percentage of success for each deformation threshold

	Wells Known to Deform		Wells Not Observed to Deform	
Threshold for Shear Deformation, %	Correctly Flagged Grid Cells, %	Correctly Flagged Wells, %	Wrongly Flagged Grid Cells, %	Wrongly Flagged Wells, %
0.05	27.3	46	0.5	26
0.04	36.4	69	0.7	38
0.03	41.0	85	1.0	46
0.022	45.4	92	1.4	52
0.01	50.1	100	2.6	77
0.006	59.2	100	8.9	84
0.002	72.8	100	27.6	91
0.0	100	100	100	100

Discussion

Out of the 16 wells observed to deform, 13 deformed in 2009 or before. This means the three wells to deform in 2010 are not incorporated into the analysis as the axial and shear strains calculated in 2009 may not be representative. Only one well deformed in 2006 (the other time step) and this means an in-depth analysis in wells that deformed could not be done solely for 2006. Instead, the analysis is carried out on wells that deformed by 2009 due to their larger quantity. Three wells deformed before 2009, and the results of 2009 were used to analyze the results from the geomechanical codes. Nonetheless, the changes in axial strain and shear strain did not vary considerable between the two time steps.

The threshold value for failure for the axial strain results showed that no well would experience casing collapse through material failure. It is important to note that the axial strain calculated along the trajectory is that of the formation. If slippage between cement and the formation is factored into the analysis, then the axial strain observed would be less than 10% of the total formation compaction as suggested by Bruno (1992). Previous work on this field showed that the casing deformations were not a result of axial contraction or elongation as the low permeability of the field meant it was unable to compact like other well-known fields such as Ekofisk or Valhall.

The threshold value used for shear strain is lower than that of axial strain. Bruno (1992) states that the bending strength of a well's casing is a magnitude lower than its compressive strength. The threshold value used for the onset of deformation by shearing was 0.022%. This is two orders of magnitude lower than the threshold used to mark the onset of failure through contraction. Since the threshold for shearing was for deformation and not failure it seems reasonable for it to be two magnitudes lower.

On a grid cell basis, the analysis showed mixed results for the calculated shear strain along well trajectories to be used to flag for deformation. To a large extent, grid cells not observed to deform were flagged correctly. However, in terms of the grid cells known to deform, more than half would not be flagged to deform. This was attributed to factors such as depth mismatches and multiple deformation intervals in two wells.

However, when analyzing well log results it can be seen that 52% of the wells not observed to deform would be wrongly flagged to deform. It is unknown whether every well was continually checked for deformation until 2010 or 2011 when the project analyzing the casing deformations ended. If some of the wells not observed to deform actually experienced deformation this could affect the results. Furthermore, it is assumed that these wells deformed through shearing. One reason for a large amount of false positives could be attributed to the wells deforming by other means. Well casings may suffer from buckling due to near wellbore instabilities caused by excessive sand production.

12 out of the 13 deformed wells analyzed were flagged to deform. Well log analysis shows that the deformation intervals were within 30 m MD of areas experiencing shear strain high enough to cause deformation. This means it was able to match accurately a flagged interval to the observed deformation.

Even though, 52% of wells not observed to deform were flagged to deform, the application of the shear strain geomechanical code cannot be seen as unsuccessful. The applied geomechanical codes do not involve casing or completion detail. One suggestion why so many wells were falsely flagged is that an appropriate casing grade and completion design is able to withstand the local deformations. Perhaps if a weaker casing grade was incorporated, then these wells may have been observed to deform. This needs to be considered as 92% of the deformed wells were correctly flagged. The application of the shear strain geomechanical code is indeed capturing useful information of the deforming rock masses along well trajectories.

The next step would be to apply the geomechanical codes and thresholds to other fields having observed casing deformation or failure. More importantly, it should be applied on fields that have different casing grades to the one used in this field to determine if there's a link between values of threshold used with different casing and completion architecture. This will ultimately decide whether the use of geomechanical codes with threshold values can predict if and when a casing can suffer deformation or failure. Lastly, by investigating a field with more known well deformations, the success of flagging deformed wells can be better understood from a statistical point of view. In this study, the high success of predicting well deformations is based on only 12 wells whereas the false flagging is based on 112 wells.

Conclusions

The strain tensor over time was the input into strain geomechanical codes that produced axial strain and shear strain along the entire trajectory of every well in a field case. Threshold values for the onset of deformation were used alongside the axial strain and shear strain results from the geomechanical codes. This flagged certain wells and depth intervals prone to deformation. These flags were compared against observed and recorded casing deformations in the field case used. The wells and depth intervals observed to deform were recorded with multi-caliper tools. Some of the main conclusions are summarized below.

- Based on previous work that concluded these wells did not deform as a result of compression or tension, the axial strain results showed that no well would fail by these mechanisms.
- The shear strain geomechanical code results, with appropriate thresholds applied, correctly predicted to a large extent the deformed wells to indeed experience deformation.
- More than half of the wells known not to observe deformation were falsely flagged to deform.

The geomechanical codes used to calculate shear and axial strain along well trajectories can be used to quickly scan on a field scale. Detailed well sector analysis can then be undertaken on flagged wells to ensure their casings can be designed to withstand the stresses and deformations in a producing reservoir. It was shown that the geomechanical codes were able to successfully flag the wells that were observed to deform, based on the thresholds used for the onset of casing deformation. However, the large amount of wrongly flagged wells shows that improvement is required to ensure the geomechanical codes can correctly predict which wells could experience deformation. Threshold values used for the onset of deformation may need to be customized to different casing and completion architecture to successfully predict deformation. It was outside the scope of this study to establish a link between the thresholds and specific casing grades and completion architecture. Further study and statistical analysis in the use of the geomechanical codes presented is required to assess the reliability of quick screening for well survivability and to identify areas of further improvement.

Nomenclature

γ = *shear strains*
ε = *strain*
ε' = *strain tensor rotated onto local well coordinates*
ε_{ws} = *shear strain*
σ = *stress*
τ = *shear stresses*
azi = azimuth angle, $^\circ$
E-Wa = axial strain
E-Ws = shear strain
G = Shear modulus, Pa
incl = inclination angle, $^\circ$
R_y = *rotation matrix about y-axis*
R_z = *rotation matrix about z-axis*
u = displacement, ft

References

Abou-Sayed, A.S., Meng, F., Noble, J.E., and Guo, Q. 2003. Modeling of Reservoir Compaction and Casing Integrity Evaluation Using Reservoir Simulation. Paper SPE 81072 proceedings of the SPE Latin America and Caribbean Petroleum Engineering Conference, Port of Spain, Trinidad and Tobago, 27-30 April. DOI: 10.2118/81072-MS.

Bickley, M.C. and Curry, W.E. 1992. Designing Wells for Subsidence in the Greater Ekofisk Area. Paper SPE 24966 proceedings of the European Petroleum Conference, Cannes, France, 16-18 November. DOI: 10.2118/24966-MS.

Beer, F.P., Johnston, E.R. and DeWolf, J.T. 2004. *Mechanics of Materials*, Third Edition. New York: McGraw-Hill.

Bruno, M.S. 1992. Subsidence-Induced Well Failure. *SPE Drilling Engineering* **7** (02): 148-152. SPE-20058-PA. DOI: 10.2118/20058-PA.

Bruno, M.S. 2001. Geomechanical Analysis and Decision Analysis for Mitigating Compaction Related Casing Damage. Paper SPE 71695 proceedings of the SPE Annual Technical Conference and Exhibition, New Orleans, Louisiana, 30 September-3 October. DOI: 10.2118/71695-MS.

Dusseault, M.B, Bruno, M.S., and Barrera, J. 1998. Casing Shear: Causes, Cases, Cures. Paper SPE 48864 proceedings of the SPE International Oil and Gas Conference and Exhibition, Beijing, China, 2-6 November. DOI: 10.2118/48864-MS.

Geertsma, J. 1973. Land Subsidence above Compacting Oil and Gas Reservoirs. *Journal of Petroleum Technology* **25** (06): 734-744. SPE-3730-PA. DOI: 10.2118/3730-PA.

Geomechanics CoE, Schlumberger. Bracknell. Author confidential.

Hamilton, J.M., Mailer, A.V., and Prins, M.D. 1992. Subsidence-induced Shear Failures above Oil and Gas Reservoirs. Paper ARMA 92-0273 proceedings of the 33th U.S. Symposium on Rock Mechanics, Santa Fe, New Mexico, 3-5 June.

Harrison, H.R. and Nettleton, T. 1997. *Advanced Engineering Dynamics*. London: Arnold.

Hilbert Jr, L.B., Gwin, R.L., Moroney, T.A. and Deitrick, G.L. 1999. Field-Scale and Wellbore Modeling of Compaction-Induced Casing Failures. *SPE Drilling and Completion* **14** (02): 92-101. SPE-56863-PA. DOI: 10.2118/56863-PA.

Ibekwe, I.A, Coker III, O.D., Fuh, G.F. and Actis, S.C. 2003. Magnolia Casing Design for Compaction. Paper SPE 79816 proceedings of the SPE/IADC Drilling Conference, Amsterdam, Netherlands, 19-21 February. DOI: 10.2118/79816-MS.

Jaeger, J.C., Cook, N.G.W. and Zimmerman, R.W. 2012. *Fundamentals of Rock Mechanics*, Fourth Edition. New Delhi: Blackwell Publishing.

Kristiansen, T.G. 2003. Valhall Field- Still on Plateau after 20 Years of Production. Paper SPE 83957 proceedings of the Offshore Europe, Aberdeen, United Kingdom, 2-5 September. DOI: 10.2118/83957-MS.

Marsden, J.R. 2010. Introduction to Near-Wellbore Rock Mechanics. Lecture, Imperial College London, United Kingdom (October, 2013)

Petrel Reservoir Geomechanics Software. 2013. Schlumberger, http://www.software.slb.com/products/platform/pages/petrel-reservoir-geomechanics.aspx.

Rahman, S.S and Chilingarian, G.V. *Casing Design Theory and Practice*. Amsterdam: Elsevier.

Telles, I. and Rodriguez, A. Mitigating Geomechanical Risks in your Assets, SIS Forum 2014.

Yudovich, A., Chin, L.Y. and Morgan D.R. 1989. Casing Deformation in Ekofisk. *Journal of Petroleum Technology* **41** (07): 729-734. SPE-17856-PA. DOI: 10.2118/17856-PA.

Appendices
Appendix A: Critical Milestones

Source	Year	Title	Authors	Contribution
Book, pg 43-62	1973	A numerical technique for predicting subsidence above compacting reservoirs based on the nucleus of strain concept	Geertsma, J. and van Opstal	Subsidence calculated at a number of points by use of the "nucleus of strain" approach
SPE 3730	1973	Land Subsidence Above Compacting Oil and Gas Reservoirs	J. Geertsma	Derived simple analytical model for compaction and subsidence (boundary element method)
SPE 17856	1989	Casing Deformation in Ekofisk	A.Yudovich, L.Y. Chin and D.R. Morgan	Developed a relationship to forecast casing failure by means of statistical methods based on field observations of failures in Ekofisk.
SPE 15469	1988	Effects of Nonlinear Reservoir Compaction on Casing Behaviour	Y.P. Chla and D.A. Bradley	Modelled frictional slippage between cement and formation. Observed that axial strain in a casing decreased with slippage.
SPE 36918	1996	The Use of Subsidence Data to Monitor Reservoir Behaviour	P.J.M Marchina	First to determine reservoir compaction from surface subsidence data that is used to characterise the pressure behaviour in areas of the reservoir where no data is available such as aquifers and undrilled blocks
SPE 56863	1999	Field Scale and Wellbore Modelling of Compaction Induced Casing Failures	L.B. Hilbert Jr, R.L. Gwinn, T.A. Moroney and G.L. Deitrick	First to develop a relationship showing what size tool can be used with the amount of casing deformation caused through shearing.
SPE 79816	2003	Magnolia Casing Design for Compaction	I.A Ibekwe, O.D Coker-III, G.F Fuh and S.C Actis	The first to publish tables of axial strain at which a casing may fail resulting from compression or tension. Incorporates four different strain ranges with mitigating strategies for casing design.
SPE 81072	2003	Modelling of Reservoir Compaction and Casing Integrity Evaluation Using Reservoir Simulation	Ahmed S. Abou-Sayed, Fanhong Meng, John E. Noble and Quanxin Guo	Coupled reservoir compaction mechanics to reservoir simulations
ARMA 92-0273	1992	Subsidence Induced Shear Failures Above Oil and Gas Reservoirs	J.M. Hamilton, A.V. Maller and M.D. Prins	Modelled shear deformations with the conclusion that failure deformation does not only occur with compacting fields but can also fail by reducing effective vertical stress through water injection.

Appendix B: Critical literature review

SPE 15469 (1988)

Effects of Nonlinear Reservoir Compaction on Casing Behavior

Authors: Chla, Y.P. and Bradley, D.A

Contribution:

Axial strain decreases between 30-40% when there is slippage between the formation and the cement of the casing. In addition, axial strain is maximum in sandstone intervals resulting from its higher shear strength than shale.

Objective of Paper:

Predict soil and casing deformation during reservoir depletion by use of a nonlinear elastic and plastic model to represent soil deformation. Slippage along the wellbore is also incorporated to simulate axial compressive strains with the final objective to provide criteria on how to improve completion design and ensure production rate is held to a safe maximum so operating limits of casing is not exceeded.

Methodology Used:

Uses a finite element model that incorporates nonlinear elastic and plastic behavior of soils in addition to frictional slippage.

Conclusion:

Shear strength in shale is much lower than sandstone. Hence, maximum axial compressive casing strain is found in the sandstone intervals. With a nonlinear elastic model, compressive axial strain reduces between 30-40% when slippage occurs between formation and cement. Finally, the use of thicker walled casing did not show a significant decrease in axial strain to warrant their benefits.

Comments:

Does not show the results of using a thicker walled casing. Axial strain results with slippage don't use a plastic model.

SPE 17856 (1989)

Casing Deformation in Ekofisk

Authors: Yudovich, A., Chin, L.Y. and Morgan, D.R.

Contribution:

First to forecast casing failure by means of statistical methods based on field observations of failures. It incorporates both near well strains and the inclination angle of the well. Threshold values for strain causing failure can be used for own project.

Objective of Paper:

Determine a relationship between reservoir compaction and casing failure by statistical analysis, finite element modelling and with analysis of deformed casings determined from log runs.

Methodology Used:

Caliper logs were run to determine which wells failed. Reservoir pressures were then computed and these were used to calculate the rock's stress and strain properties. A link between failed wells, near well strains and well inclination angle was subsequently made.

Conclusion:

Can limit casing failure by reservoir compaction by pressure maintenance, drill at high deviated angles and use largest diameter of casing possible in the well.

Comments:

States that wells with higher inclination angles fail at higher incremental strains. This statement is questionable and the reasons for this statement are not explained in detail.

SPE 14985 (1989)

Evaluation of Reservoir Compaction and Its Effects on Casing Behavior

Authors: Chla, Y.P. and Bradley, D.A

Contribution:

Frictional slippage is most likely to occur between cement and formation as the shear strength between casing and cement is much greater than the bond between cement and formation. Shear strength is weakest between shale and cement. As a result, maximum axial casing strain is found in sand reservoirs. When slippage was modelled, maximum axial strain decreased from 1.9% (no slippage) to 1.3%.

Objective of Paper:

Evaluate reservoir compaction around a wellbore and examine its effects on casing deformation during the depletion of over pressured reservoirs. The ultimate objective is to have a better understanding of the distribution of casing stress and strain, the effects of slippage between cement and formation, the effects of physical properties of sediments on casing deformation and casing failure mechanisms.

Methodology Used:

A finite element model was used to simulate sediment deformation, fluid flow and casing deformation all at once.

Conclusion:

Depletion in an under consolidated, over pressured reservoir can cause formation compaction in the sand reservoir but also in neighboring shale formations. The maximum axial compressive stresses that cause yield failure were seen to occur 7 ft above and below each depleted reservoir. Finally, sensitivity tests showed that casing axial strain increased when the Young's Modulus of the formation decreases and with an increased rate in production.

Comments:

Simulation was based on sediments with an isotropic stiffness whereas in reality it doesn't. As a result, the axial strains measured with the FEM analysis may not be an accurate representation. Furthermore, the FEM model assumes the sediment to be linear elastic and in reality are going to behave plastically. Nonetheless, the results are interesting because of the sensitivity analysis incorporated.

SPE 56863 (1999)

Field Scale and Wellbore Modeling of Compaction Induced Casing Failures

Authors: Hilbert Jr, L.B., Gwinn, R.L., Moroney, T.A. and Deitrick, G.L.

Contribution:

Provides an equation relating maximum tool length able to pass through various stages of tubing deformation through shearing. Provides a deformation amount over a depth interval to provide a threshold for onset of failure in tubing.

Objective of Paper:

To use an elasto-plastic finite element geomechanical model to model the compaction in a high porosity field. After which, wellbore scale finite element model is analyzed to predict when casing damage could occur. The prediction of casing failure will be compared to actual events in the field's history.

Methodology Used:

Two dimensional geomechanical field scale models were created by the use of ABAQUS. This program uses a Drucker-Prager shear failure criterion incorporated with a Cap plasticity model.

Conclusion:

The FEM provided accurate calculations of reservoir compaction and was able to predict casing damage. Predicted shear deformations and to determine when tools would become stuck in the bent tubing.

Comments:

The FEM provided accurate magnitudes for compaction. However, nothing is stated about the comparison between horizontal movement. The final conclusion was that the model was 'moderately successful'. There are no statistics of the success and this may question the usefulness of the threshold value for the onset of failure being used from this paper. Finally, the interface between casing and formation is not modelled so casing damage prediction may be over predicted.

SPE 71695 (2001)

Geomechanical Analysis and Decision Analysis for Mitigating Compaction Related Casing Damage

Authors: Bruno, M.S.

Contribution:

Not much as author summarizes current techniques. Provides understanding of simple analytical solutions (to calculate subsidence, axial compressive strain and shear stress), 2D numerical modelling and 3D reservoir modelling. Highlights that 3D wellbore modelling is required to assess different completions designs or mitigate casing damage at a given location. This involves the wellbore region to be discretized to a very fine scale separately.

Objective of Paper:

Details of casing damage observations across different fields and the geomechanical analysis techniques applied to evaluate the casing damage and strategies to mitigate these damages. This paper also describes a quantitative decision analysis process to estimate economic value of different completion designs to limit casing damage.

Methodology Used:

Uses case examples from Sandia National Laboratories who analyzed casing damage at the Lost Hills Field. Also uses commercial software (FLAC3D).

Conclusion:

Summarizes main casing damage mechanisms. Analytical solutions should be used as initial screening tools with 2D or 3D finite element geomechanical models to be used to assess formation deformation and evaluate casing damage risks. Furthermore, 3D wellbore models should be used to evaluate the possibilities of shearing.

Comments:

Not feasible to analyze well survivability field wide with 3D techniques. The detail required for the wellbore scale model is time consuming and requires expertise to input appropriate completion details.

SPE 72060 (2001)

Casing Shear: Causes, Cases, Cures

Authors: Dusseault, M.B., Bruno, M.S. and Barrera, J.

Contribution:

Investigated that shearing of a well is common on the shoulders of a reservoir. Also, strengthening of the casing-cement does not prevent shearing of a well as it cannot resist the slipping interfaces. The stiffer a casing-cement system, the more likely it will attract stresses and fail.

Objective of Paper:

Highlights main cause of casing failure (shearing of weak lithology interfaces in the overburden) and main mitigation strategies to avoid total casing failure.

Methodology Used:

Uses slip criteria (Mohr-Coulomb criterion) to determine when lithology interfaces will fail.

Conclusion:

Casing shear mainly occurs because of weak sediments but can also be caused by reactivation of old faults, high pressure injection or massive solids production. The only way to quantify these causes is through 3D geomechanical modelling.

Comments:

Does not explain how the internal friction coefficient between two interfaces is determined for use with the Mohr-Coulomb failure criteria. Internal friction coefficient is usually of one material internally but for assessing shear failure, the internal friction coefficient is required between two materials.

SPE 79816 (2003)

Magnolia Casing Design for Compaction

Authors: Ibekwe, I.A., Coker-III, O.D., Fuh, G.F. and Actis, S.C.

Contribution:

Design strategy is based on reservoir compaction in the Gulf of Mexico. Two tables showing compaction strain and stretch strain at various inclination angles are used to guide the strategy. They have four key regions going from green to red describing the associated risks on the well with increasing strain.

Objective of Paper:

Estimates reservoir compaction and overburden stretch. This was used to look at the effect of tension on the casing in the overburden and how reservoir compaction deforms the casing. This investigation was used to design casings appropriately.

Methodology Used:

A model was used to model stress and strain in a depleting reservoir that looked at a fully communicating reservoir and a highly compartmentalized reservoir. Both stiff and soft cap rock models were used for both cases.

Conclusion:

It was found that the largest strains developed immediately above the compacting reservoir with it decreasing by the square of the distance away from the reservoir. It was determined that if the casing and formation are not bound uniformly, then the high tension may reduce the collapse resistance of the pipe and can collapse hydrostatically.

Comments:

Mistake in the soft cap model equations that were used. Accounts for the D/t ratio of the wells and is particularly useful to identify maximum axial strain before failure for a common casing design.

SPE 117773 (2008)

A Look into Casing Deformation to Plastic Behavior of Formations

Authors: Sunal, O., Bilgesu, H.I., Heasley, K.A. and Tulu, I.B.

Contribution:

Focusing on casing failure caused by salt and shale formations

Objective of Paper:

Investigate the behavior of plastic formations and its impact on horizontal stresses on the casing in a wellbore. Look at different formation characteristics, cement thickness, off-center configuration and anisotropic stress conditions.

Methodology Used:

Uses a finite difference program (FLAC 3D computer code). Drucker-Prager material model to simulate behavior of steel. Mohr-Coulomb model used to model the cement with strain-softening model and formations

Conclusion:

Salt and shale tend to fail locally first rather than dissipate stress. Deformation occurs faster in salt than in shale and leads to earlier casing failure for salt formation. Higher cement thickness increases resistance to casing collapse. Deformation on casing was faster under anisotropic stress conditions.

Comments:

Looks at casing loading caused by salt and shale beds. When shale is under high pressure, it acts similar to salt.

ARMA 92-0273 (1992)

Subsidence Induced Shear Failures above Oil and Gas Reservoirs

Authors: Hamilton, J.M., Miller, A.V. and Prins, M.D.

Contribution:

Shear failure does not necessarily occur from compaction of the reservoir. Slippage along a weak layer can also occur if an increased pore pressure decreases the effective normal vertical stress. Furthermore, shale with more active clay minerals have lower friction angles and are more prone to slippage.

Objective of Paper:

To use finite element models to replicate what Bruno (1990) demonstrated, in which flexure above a compacting reservoir builds shear stresses along the flanks of a reservoir. This can cause shear failures and slippage along weak interfaces. The Wilmington and Ekofisk oil fields will be modelled where the amount of subsidence and shear deformation is then compared to literature values.

Methodology Used:

The ABAQUS finite element program was used where subsidence histories are modelled based on material properties and reservoir pressure decline information from literature. Weak layers were simulated with frictional sliding interface elements in which were determined by the friction coefficient and vertical effective stress with cohesion neglected. Friction angles used were between 10 to 20 degrees.

Conclusion:

Overburden shearing was a direct result of increased pore pressure in the shale interval. This reduced the effective vertical stress in which decreased the sliding resistance of the shale. From the Ekofisk model, it showed that with normal pore pressure no slippage would have occurred with a subsidence of 15 ft. It was also found that a stiffer overburden leads to a larger concentration of shear strain on the weak shale layer.

Comments:

Axisymmetric models were used. Furthermore, an elastic model was used. These model attributions are not applicable to the test case field model where the field is not elliptical in shape like Ekofisk. Hence, care needs to be taken when comparing slippage with the fields discussed and with that of the test field case used for proxy validation. Finally, slippage amounts of stated but not slippage amounts where failure starts.

Appendix C: Coupled reservoir-geomechanical model simulation

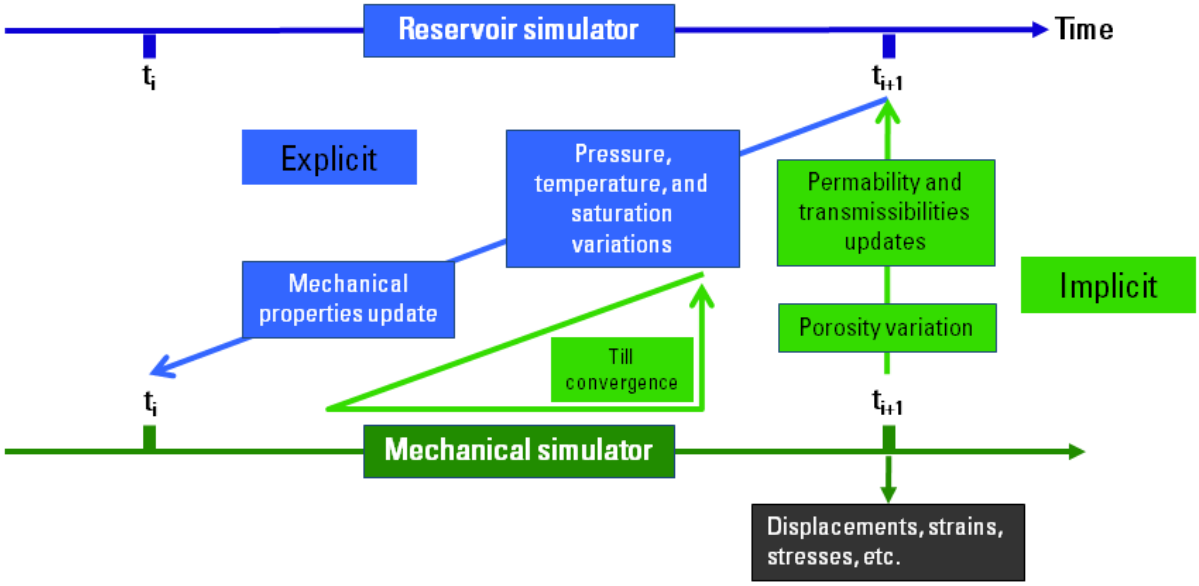

Figure 19: Overview of the coupled simulation process between a reservoir simulation and a geomechanical model. It shows how the reservoir simulator will calculate the changes in pressure, temperature and temperature over one time step and input the results into the previous time step in the geomechanical model to update mechanical properties and the reservoir's permeability.

Appendix D: Mathematical overview of the geomechanical simulator, VISAGE

VISAGE uses a finite element method to compute the changes in stresses and strains in the geomechanical model. To do this, it uses a visco-elastic model to represent the behavior of the rock. Simple elastic theory is not used as it does not display the true behavior of rock when subjected to three dimensional stresses. A stress-strain curve from triaxial tests has shown to be a non-linear relationship where strain is irrecoverable.

With the elasto-plastic model, rock behavior is elastic, where strain is recoverable, and becomes plastic once the stresses exceed the failure criteria of the rock. These failure criteria will be a function of the rock's cohesion strength and its internal friction angle.

The 3D elasticity theory shows the fundamentals of the model used and helps to understand where each parameter is derived from Eq. A 1and Eq. A 2 are the stress and strain tensors. In Eq. A 1 σ_{xx}, σ_{yy} and σ_{zz} are the normal stresses and τ_{xy}, τ_{xz} and τ_{yz} are the shear stresses. The normal strains in Eq. A 2 are ε_{xx}, ε_{yy} and ε_{zz} and the shear strains are γ_{xy}, γ_{xz} and γ_{yz}. For linear elasticity, the shear and strain have a linear relationship as seen in Eq. A 3. Eq. A 4 is the displacement vector that is linked with strain through Eq. A 5 and Eq. A 6. Lastly, the external forces acting on a body and the internal stresses are represented by the equilibrium equations of stress in Eq. A 7, Eq. A 8 and Eq. A 9. Here, ρF is the body force per unit volume. The right hand sides of these equations are zero because of the rock being in static equilibrium or if there are any displacements, are slow occurring. To solve for all the parameters in the elastic theory, a finite element model is used

$$\sigma = \begin{bmatrix} \sigma_{xx} & \tau_{xy} & \tau_{xz} \\ \tau_{yx} & \sigma_{yy} & \tau_{yz} \\ \tau_{zx} & \tau_{zy} & \sigma_{zz} \end{bmatrix}$$

Eq. A 1

$$\varepsilon = \begin{bmatrix} \varepsilon_{xx} & \gamma_{xy} & \gamma_{xz} \\ \gamma_{yx} & \varepsilon_{yy} & \gamma_{yz} \\ \gamma_{zx} & \gamma_{zy} & \varepsilon_{zz} \end{bmatrix}$$

Eq. A 2

$$\sigma = D \times \varepsilon$$

Eq. A 3

$$u = \begin{bmatrix} u(x,y,z) \\ v(x,y,z) \\ w(x,y,z) \end{bmatrix}$$

Eq. A 4

Strain-displacement relationship:

$$\varepsilon_x = \frac{\partial u}{\partial x}\ ;\ \varepsilon_y = \frac{\partial v}{\partial y}\ ;\ \varepsilon_x = \frac{\partial w}{\partial z}$$

Eq. A 5

$$\gamma_{xy} = \frac{\partial v}{\partial x} + \frac{\partial u}{\partial y};\ \gamma_{yz} = \frac{\partial w}{\partial y} + \frac{\partial v}{\partial z};\ \gamma_{zx} = \frac{\partial u}{\partial z} + \frac{\partial w}{\partial x}$$

Eq. A 6

Equations of stress equilibrium:

$$\frac{\partial \sigma_x}{\partial x} + \frac{\partial \tau_{xy}}{\partial y} + \frac{\partial \tau_{xz}}{\partial z} + \rho F_x = 0$$

Eq. A 7

$$\frac{\partial \tau_{xy}}{\partial x} + \frac{\partial \sigma_y}{\partial y} + \frac{\partial \tau_{yz}}{\partial z} + \rho F_y = 0$$

Eq. A 8

$$\frac{\partial \tau_{xz}}{\partial x} + \frac{\partial \tau_{yz}}{\partial y} + \frac{\partial \sigma_z}{\partial z} + \rho F_z = 0$$

Eq. A 9

Source: Petrel Reservoir Geomechanics manual and Fundamentals of Rock Mechanics

Appendix E: Overview of current method in determining well survivability

Firstly, a geomechanical model is populated with material properties, stresses and deformations of the rock. This is done by coupling a reservoir simulation to a geomechanical model. To analyze the survivability of a wellbore's casing, a well sector model is extracted from the field model. This wellbore sector only includes the trajectory of one well and contains the pre-drill reservoir conditions. Then a hole is excavated along the well's trajectory with the mud weight pressure applied within the excavation. The stresses around the well are then re-evaluated. After which, the casing and cement properties are applied to a finite element grid with a concentric pattern around the excavation. These properties are applied at appropriate diameters along the trajectory to represent the completion of the well. The final part of the analysis involves depleting the pore pressure in a number of time steps and calculating the changes in stresses and strains. Both elastic and plastic strains are investigated along with the incremental displacements to determine at what interval a well may suffer failure. Figure 20 shows the diagrammatic overview of this process.

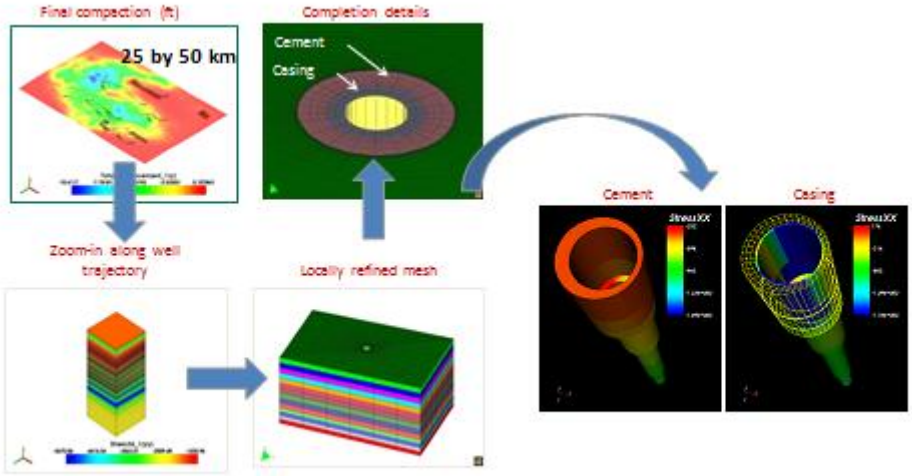

Figure 20: Diagrammatic overview of the current method in determining well survivability (image courtesy of Schlumberger).

Appendix F: Mathematical detail of the shear and axial strain proxy

The proxy used to calculate axial and shear strain along a well's trajectory will be used to determine if a well is experiencing large tension or compression strains and if there is shearing perpendicular to the well's path. Both the axial strain and shear strain are calculated at a sampling rate of every 5 ft MD.

The strain tensor, Eq. A 10, in each cell block in the geomechanical model is used. This strain tensor is first aligned with the well's trajectory. To do this, a rotation matrix defined by the well's inclination and azimuth angles is defined. It is rotated along the y-axis by its inclination and the z-axis by its azimuth at each sampling point along a well. These expressions are shown in Eq. A 11 and Eq. A 12 respectively. The transpose of this matrix is then multiplied by the strain tensor to provide a new strain tensor in terms of a local coordinate system along the well's trajectory. Eq. A 13 shows mathematics required to obtain the new strain tensor, ε'.

$$\tilde{\varepsilon} = \begin{pmatrix} \varepsilon_{xx} & \gamma_{xy} & \gamma_{xz} \\ \gamma_{yx} & \varepsilon_{yy} & \gamma_{yz} \\ \gamma_{zx} & \gamma_{zy} & \varepsilon_{zz} \end{pmatrix}$$

Eq. A 10

$$R_y(incl) = \begin{pmatrix} \cos(incl) & 0 & -\sin(incl) \\ 0 & 1 & 0 \\ \sin(incl) & 0 & \cos(incl) \end{pmatrix}$$

Eq. A 11

$$R_z(azi) = \begin{pmatrix} \cos(azi) & \sin(azi) & 0 \\ -\sin(azi) & \cos(azi) & 0 \\ 0 & 0 & 1 \end{pmatrix}$$

Eq. A 12

$$\varepsilon' = \left[R_y(incl) \times R_z(azi)\right]^T \times \tilde{\varepsilon} = \begin{pmatrix} \varepsilon'_{xx} & \gamma'_{xy} & \gamma'_{xz} \\ \gamma'_{yx} & \varepsilon'_{yy} & \gamma'_{yz} \\ \gamma'_{zx} & \gamma'_{zy} & 128 \text{ wel} \end{pmatrix}$$

Eq. A 13

Failure by Tension or Compression

After rotation, the z-component of the strain tensor is aligned with the well's trajectory. This means the axial strain can be found from the zz-strain component of ε_{zz}' . To ensure this proxy was correctly applied, a vertical well was created to compare its axial strain with the vertical component of the original strain tensor. It was observed that both were equal. Furthermore, in regards to sign convention, a positive axial strain represents compression whilst a negative axial strain indicates tension.

Failure by Shearing

The proxy that calculates the shear strain of a well uses the γ_{xz} and γ_{yz} of the strain tensor. The reason being is that the shear strain is in relation to the z-component of the strain tensor. After which, the two values are normalized to provide the shear strain along a well's trajectory. **Figure 21** shows both components of the strain tensor. It helps to understand that the angle between the two components, in relation to the z'-axis, is at a right angle. As a result, Pythagoras is used to calculate the shear strain, ε_{ws} , in Eq. A 14.

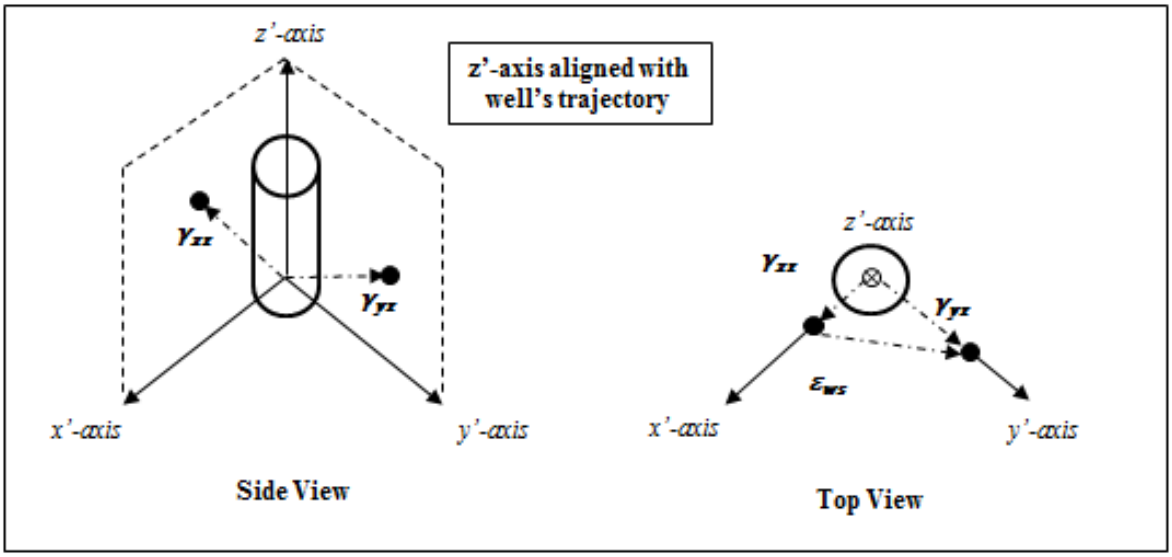

Figure 21: After the z-axis is aligned with the well's trajectory, the shear strain is comprised of the z'-x' and z'-y' coordinate planes.

$$\varepsilon_{ws} = \sqrt{{\gamma'_{xz}}^2 + {\gamma'_{yz}}^2}$$

Eq. A 14

Appendix G: Pseudo code and program code for the strain proxy and its implementation

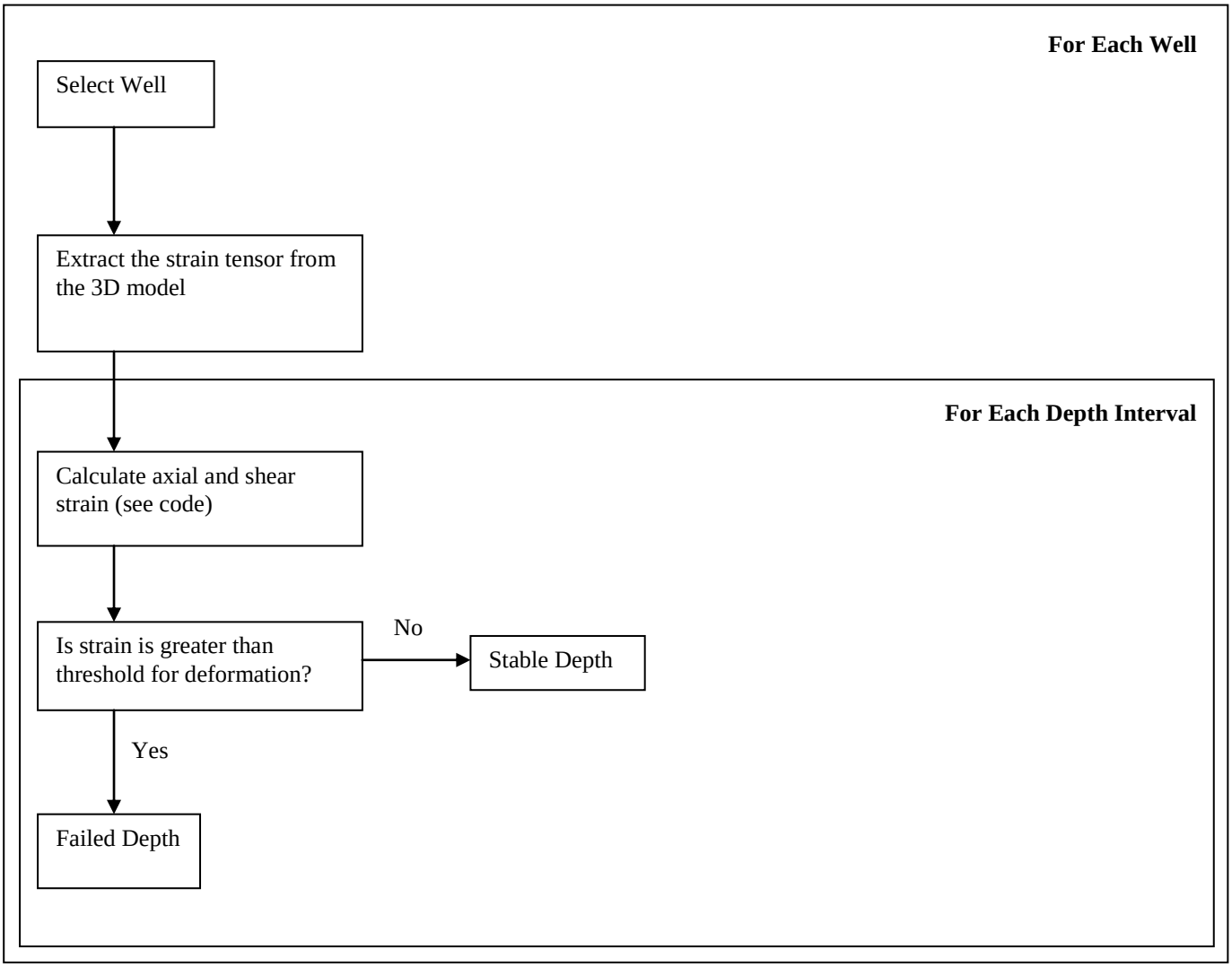

Figure 22: Pseudo code explaining an overview of the axial and shear strain proxies.

```
function Well_Integrity_QL(well_W, SXX,SYY,SZZ,Txy,Tyz,Tzx)

  Inc = GetData(well_W,'INCL')
  Azi = GetData(well_W,'AZIM')
  AngleUnit='rad'
  Inc.Unit        =AngleUnit
  Azi.Unit        =AngleUnit

% Create output logs (unless they already exist)
Sampling_log = CreateNew(well_W, Inc)
%
E_Wa         = CreateNew(well_W, Sampling_log)
E_Ws         = CreateNew(well_W, Sampling_log)

E_Wa.Template     = 'Strain'
E_Ws.Template     = 'Strain'
%
%
```

```
% Generate well logs from grid cells - Output format controlled by right-hand
side's format
SXX_Log = SXX * (1+0*Sampling_log)
SXX_Log.Unit = SXX.Unit
SXX_Log.Template = SXX.Template
SYY_Log = SYY * (1+0*Sampling_log)
SYY_Log.Unit = SYY.Unit
SYY_Log.Template = SYY.Template
SZZ_Log = SZZ * (1+0*Sampling_log)
SZZ_Log.Unit = SZZ.Unit
SZZ_Log.Template = SZZ.Template
Txy_Log = Txy * (1+0*Sampling_log)
Txy_Log.Unit = Txy.Unit
Txy_Log.Template = Txy.Template
Tyz_Log = Tyz * (1+0*Sampling_log)
Tyz_Log.Unit = Tyz.Unit
Tyz_Log.Template = Tyz.Template
Tzx_Log = Tzx * (1+0*Sampling_log)
Tzx_Log.Unit = Tzx.Unit
Tzx_Log.Template = Tzx.Template
%
%Publish(SXX_Log,SYY_Log,SZZ_Log,Txy_Log,Tyz_Log,Tzx_Log,PP_Log,POISSONR_Log,TST
R_Log)
%
% Loop over the sampling log's depths

   for i=1:Sampling_log.Count
   %
   % Convert from X pointing East,  Y pointing North and Z pointint upward
   %         to   X pointing North, Y pointing East  and Z pointint downward
   XXl=SYY_Log(i)
   YYl=SXX_Log(i)
   ZZl=SZZ_Log(i)
   XYl=+1.0*Txy_Log(i)
   YZl=-1.0*Tzx_Log(i)
   ZXl=-1.0*Tyz_Log(i)

   %%%%%%%%%
   %Calculate the strains axial and perpendicular to the well axis
   [E_Waxial, E_Wshear] =
Create_Well_strains(Inc(i),Azi(i),XXl,YYl,ZZl,XYl,YZl,ZXl)
   E_Wa(i)       = E_Waxial
   E_Ws(i)       = E_Wshear
     end

%
% Publish  results
%
Publish(E_Wa)
Publish(E_Ws)

end



function [E_Wa,E_Ws] = Create_Well_strains(Inc,Azi,XX,YY,ZZ,XY,YZ,ZX)
%
```

```
NEV        =zeros(3,3)
TOH        =zeros(3,3)
ROT_nev_toh=zeros(3,3)
dummy      =zeros(3,3)
%
% Initialization
NEV(1,1)=XX
NEV(1,2)=XY
NEV(1,3)=ZX
NEV(2,1)=NEV(1,2)
NEV(2,2)=YY
NEV(2,3)=YZ
NEV(3,1)=NEV(1,3)
NEV(3,2)=NEV(2,3)
NEV(3,3)=ZZ
%
% Rotation from North, East, vertical_down
% to well radius through TOH, well tangent, well axis down
ROT_nev_toh(1,1)=Cos(Inc)*Cos(Azi)
ROT_nev_toh(1,2)=Cos(Inc)*Sin(Azi)
ROT_nev_toh(1,3)=-1.0*Sin(Inc)
ROT_nev_toh(2,1)=-1.0*Sin(Azi)
ROT_nev_toh(2,2)=Cos(Azi)
ROT_nev_toh(2,3)=0.0
ROT_nev_toh(3,1)=Sin(Inc)*Cos(Azi)
ROT_nev_toh(3,2)=Sin(Inc)*Sin(Azi)
ROT_nev_toh(3,3)=Cos(Inc)
%
% Transpose of the rotation matrix
ROT_nev_toh_t=transpose(ROT_nev_toh)
%
% Matrix multiplications
dummy=mtimes(ROT_nev_toh,NEV)
TOH  =mtimes(dummy,ROT_nev_toh_t)
%

%
E_Wa        = TOH(3,3)
E_Ws        = Abs(Sqrt(TOH(1,3)*TOH(1,3) + TOH(2,3)*TOH(2,3)))
%

end
%%%%%%%%
```

Appendix H: Strain Threshold Values for Start of Deformation and Failure

Table 2: Failure threshold values for contracting strain

Onset of Failure from Compression			
SPE Paper	**Axial Strain**	**Field**	**Comments**
17856	**>5%**	Ekofisk	Failure occurred at 5% near well incremental strain. Slippage between formation and cement was identified. Hence, casing may have failed at lower strains.
81072	**3-5%** **3%** *(for tubing)*	Based on Gulf of Mexico and North Sea fields.	Observed in field cases.
20058	**0.3%-0.7%**	Unknown	Conservative estimate for critical strain for steel.
79816	**1.0%-2.5%**	Magnolia	Probability of failure increases and is considerable beyond 1%.

Table 3: Failure threshold values for elongating strain

Onset of Failure from Tension			
SPE Paper	**Axial Strain**	**Field**	**Comments**
79816	**1.0%-2.5%**	Magnolia	Probability of failure increases and is considerable beyond 1%.

Table 4: Deformation threshold values for shearing strain

Onset of Failure from Shearing			
SPE Paper	**Shear Strain**	**Field**	**Comments**
-	**0.022%**	Test Case	Based on observations and only applicable for onset of deformation.
56863	**4.2%**	Belridge	Shear strain calculated at where permanent bending of tubing occurs.

Appendix I: Well log results of axial and shear strain

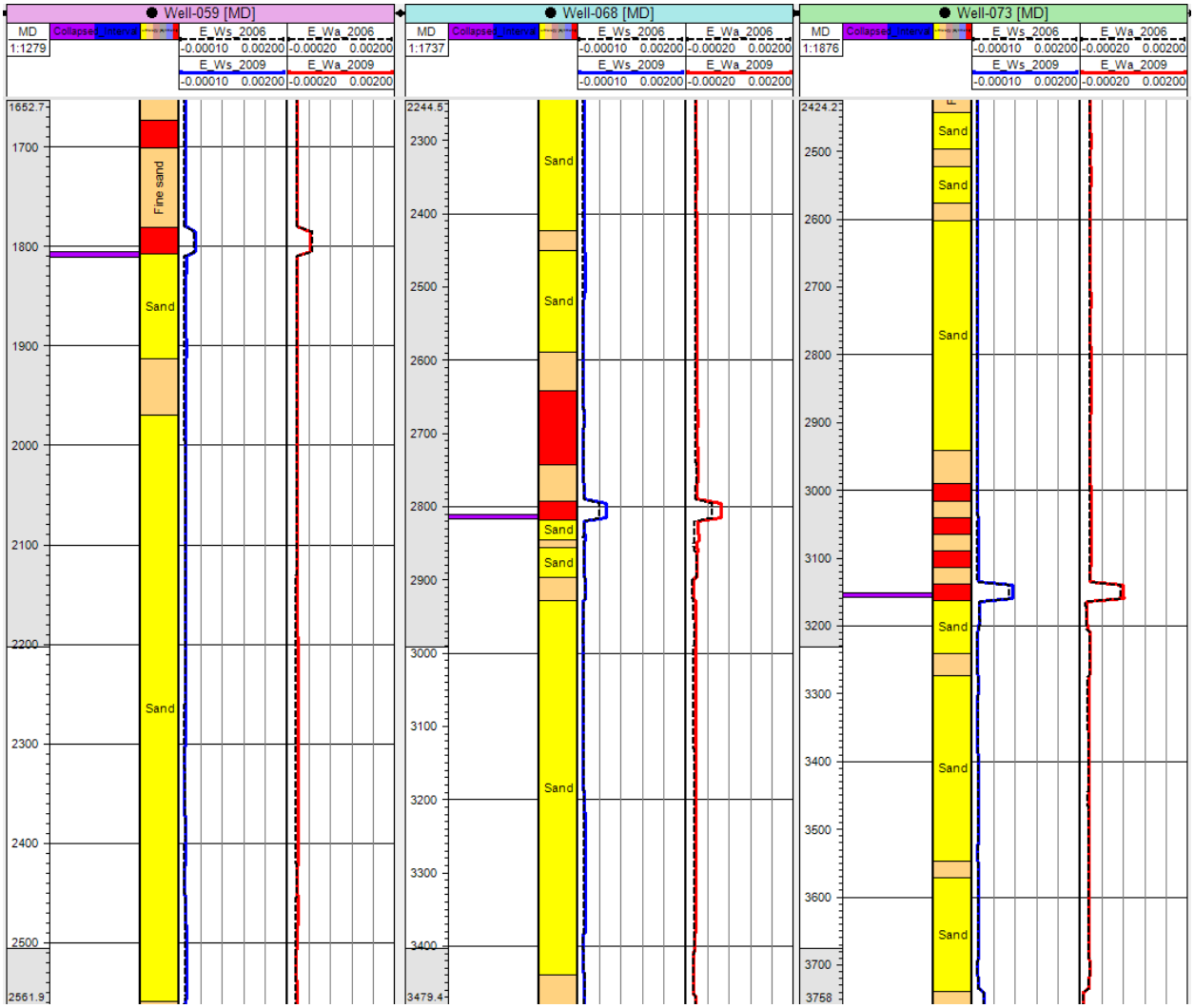

Figure 23: Shear strain and axial strain results for Well-059, Well-068 and Well-073.

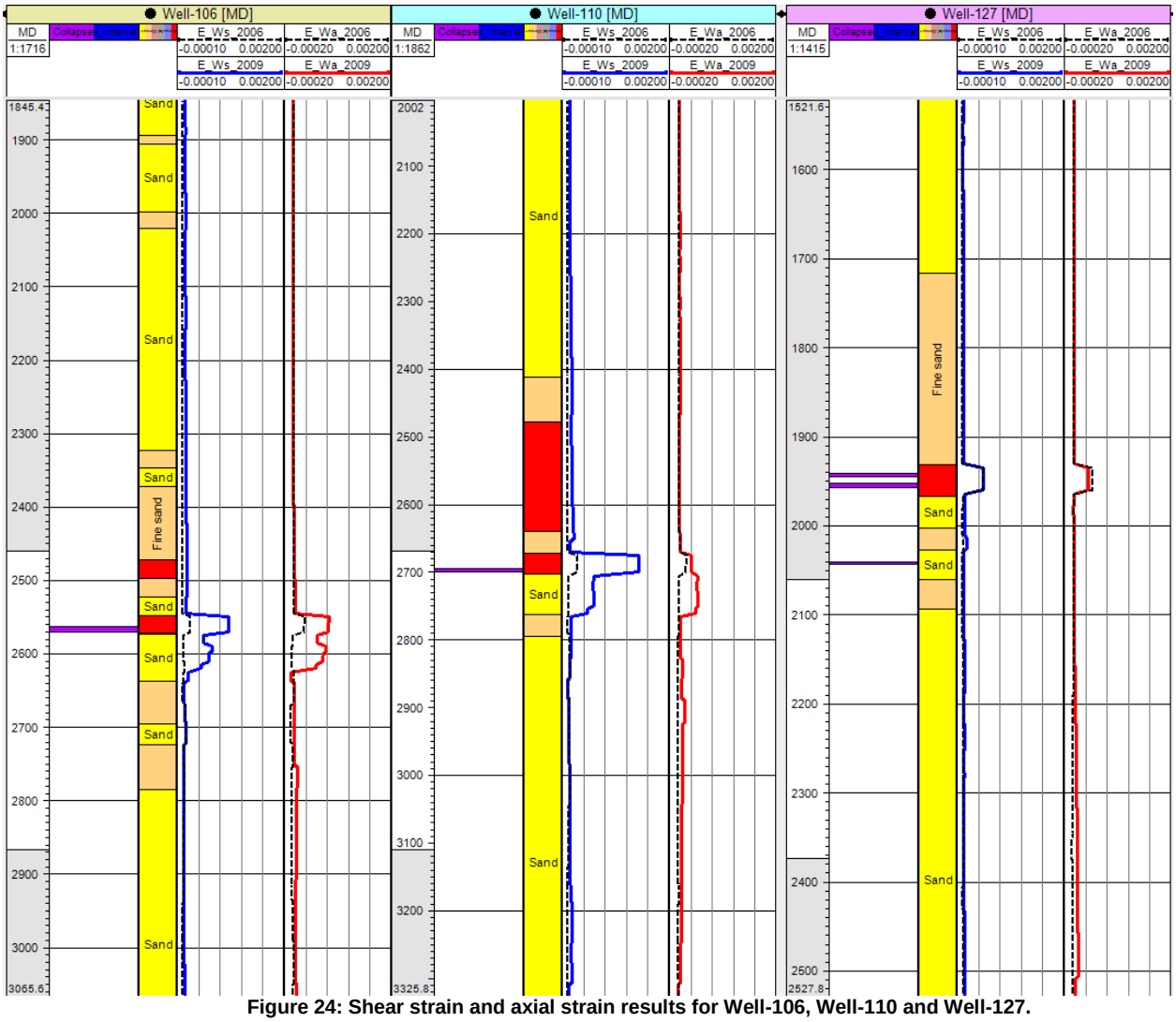

Figure 24: Shear strain and axial strain results for Well-106, Well-110 and Well-127.

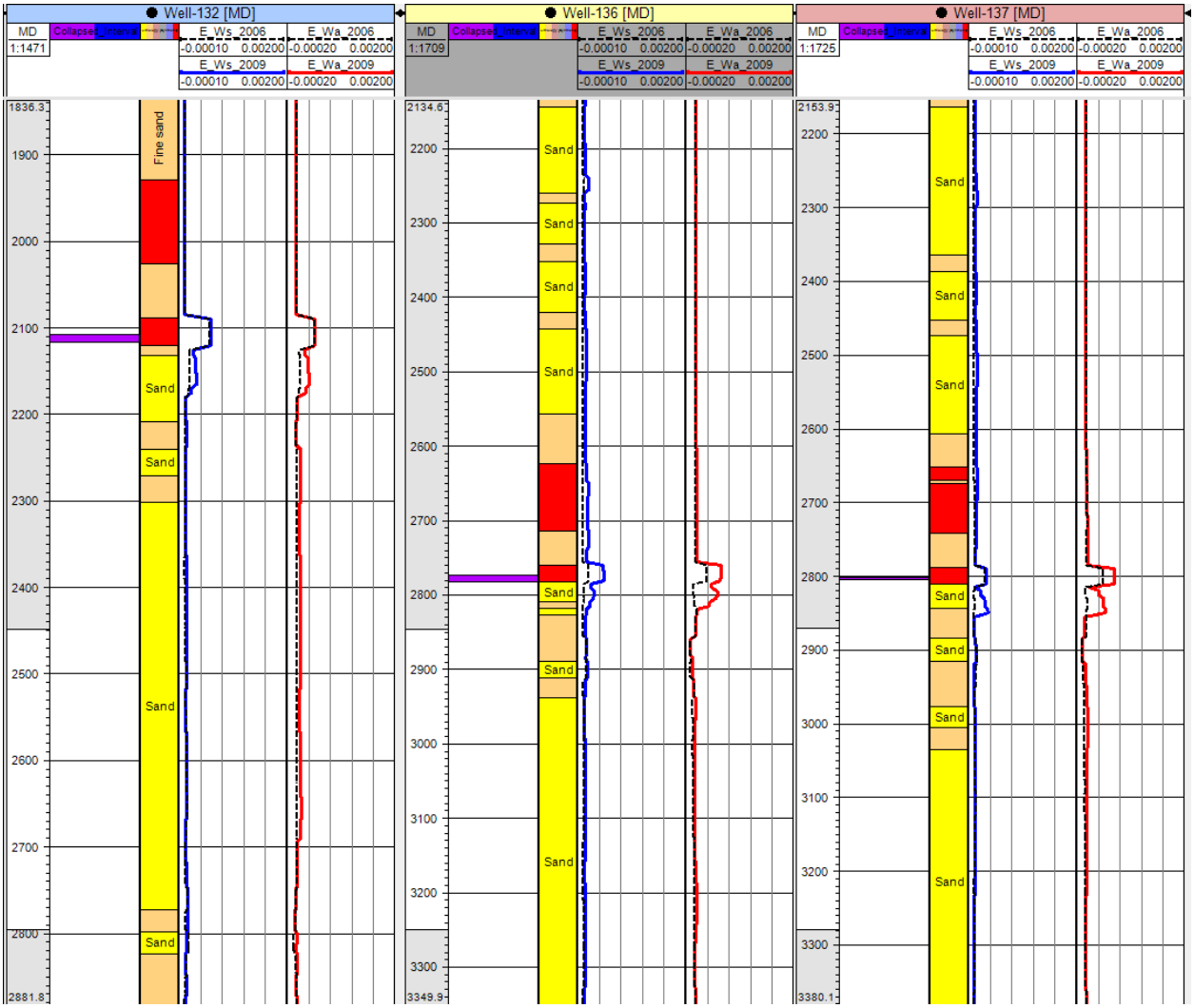

Figure 25: Shear strain and axial strain results for Well-132, Well-136 and Well-137.

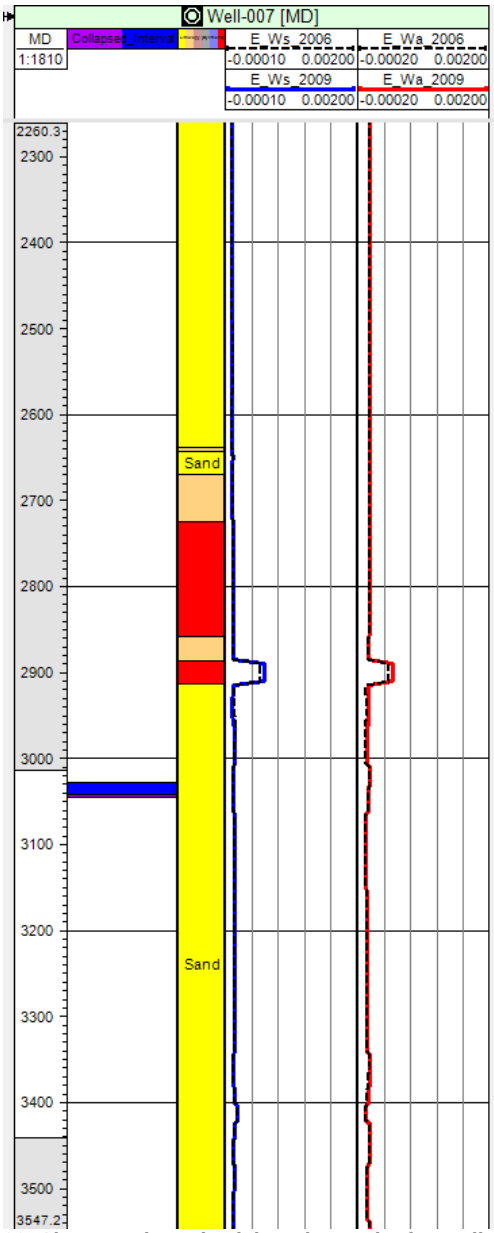

Figure 26: Shear strain and axial strain results for Well-007.

Appendix J: Effect of well inclination on shear strains in two dimensions

The stresses applied on a grid cell are examined. The stresses acting normal to a surface are known as the normal stress (σ_3 and σ_1 for 2-dimensions). When a plane is inclined, then it will experience a normal stress to it, σ_a, and a shear stress, τ_a (Marsden, 2010). The relationship between the stresses experienced on an inclined plane is shown by a Mohr's circle in **Figure 27**. If the plane, a, is horizontal then only the principal stresses are occurring. Once this plane inclines, shear stresses are induced. The maximum occurring shear stress occurs at 45˚.

Mohr's circle can be applied to strain as the transformation equations for plane strain and plane strain are in the same form (Beer et al, 2004). **Figure 28** shows Mohr's circle applied with strain. The minimum and maximum values of principal strains are on the horizontal axis. If the plane on where strain acts rotates, then shear strains are induced. If the shear deformation causes rotation clockwise, then the positive half of the Mohr's circle is used. Shear deformations occurring counterclockwise uses the section of Mohr's circle below the principal strain axis, ε. The maximum shear strain occurs when the plane is at 45˚ where $2\theta_p$ equals 90˚ in Figure 28. In linear elastic isotropic cases, the stress and strain are directly proportional by Hooke's Law in Eq. A 15 (Jaeger et al, 2012).

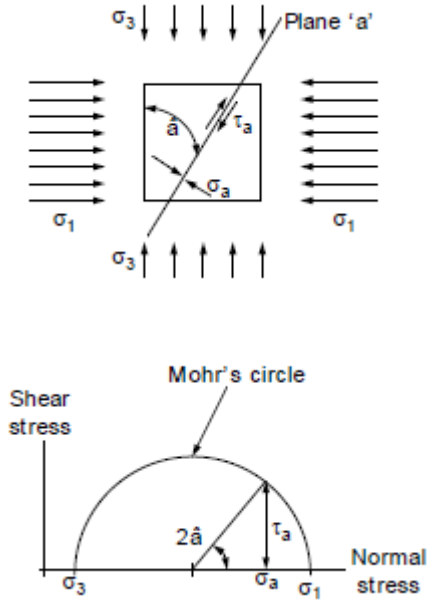

Figure 27: Relationship between principal stresses and induced shear stresses on an inclined plane represented by Mohr's circle (Marsden, 2010).

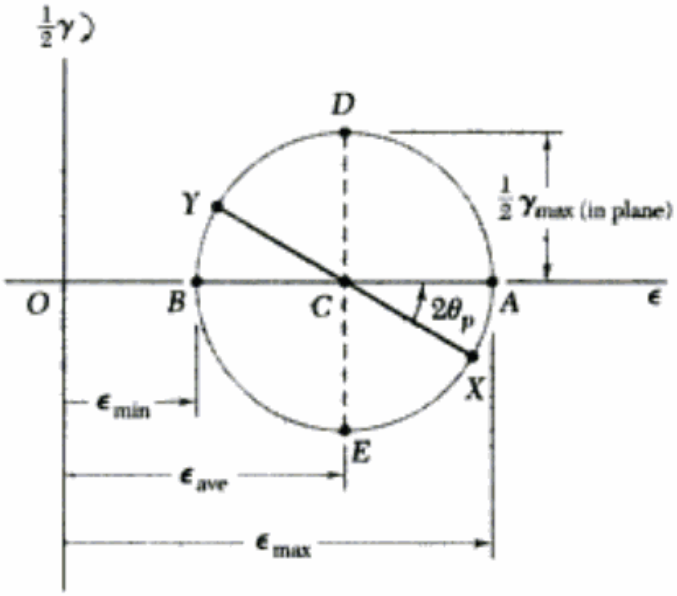

Figure 28: Mohr's circle extended to plane strain (Beer et al, 2004).

$$\tau_{xy} = 2G\gamma_{xy}, \quad \tau_{xz} = 2G\gamma_{xz}, \quad \tau_{yz} = 2G\gamma_{yz}$$

Eq. A 15